A physically-based method for predicting high temperature fatigue crack initiation in P91 welded steel

A physically-based method for predicting high temperature fatigue crack initiation in P91 welded steel

Jinbiao Zhou[1,3], Richard A. Barrett[1,2,3], Sean B. Leen[1,2,3]

[1]Mechanical Engineering, College of Engineering and Informatics, NUI Galway.

[2]Ryan Institute for Environmental, Marine and Energy Research, NUI Galway.

[3]I-Form Advanced Manufacturing Research Centre, Ireland.

Abstract

A methodology is presented for physically-based prediction of high temperature fatigue crack initiation in 9Cr steels, with a focus on material inhomogeneity due to welding-induced metallurgical transformations. A modified form of the Tanaka-Mura model for slip band formation under cyclically-softening conditions is implemented in conjunction with a physically-based unified cyclic viscoplasticity constitutive model. The physically-based constitutive model accounts for the key strengthening mechanisms, including precipitate hardening and hierarchical grain boundary strengthening, successfully predicting cyclic softening in 9Cr steels. A five-material, finite element model of a P91 cross-weld test specimen, calibrated using the physically-based yield strength and constitutive models, successfully predicts the measured detrimental effect of welding on high temperature low-cycle fatigue crack initiation for P91 cross weld tests, via the modified Tanaka-Mura models. A key finding of the current work is the requirement to adopt an energy-based Tanaka-Mura method to account for cyclic softening in 9Cr steels, with packet size as the critical length-scale for slip band formation. The work demonstrates the significant effect of highly flexible operation on the service life of welded connections.

Keywords: Crack initiation; High temperature fatigue; Microstructure; P91 steel; Weldments

1. Introduction

Since the 1970s, with the outbreak of the energy crisis, while improving the traditional industrial development mode, modern industry began to develop in the direction of economy, security and sustainability. At the same time, in recent years, with the continuous warming of global temperature, the "greenhouse effect" is becoming more and more serious and the petrochemical and energy power industries are developing towards higher temperature and higher pressure. This will inevitably pose many new challenges to the safe design and life

analysis of high temperature key components, requiring materials and structures, such as welded connections, which are resistant to thermal fatigue, creep-fatigue and thermo-mechanical fatigue. A key obstacle to safe design of such plant, to protect personnel, assets and the environment, is the need for appropriate structural integrity assessment methods. In the face of frequent start-up, shut-down and large-scale load variations, increased occurrence of repeated thermal and mechanical stresses will lead to increased low cycle fatigue damage [1]. P91 steel is a 9Cr1Mo nano-strengthened, tempered martensitic alloy for high-temperature applications, specially developed for the power generation industry due to its high thermal conductivity and low thermal diffusion coefficient [2]. The microstructure of P91 is hierarchical in nature, with numerous different associated salient length-scales (e.g. high and low-angle grain boundaries). In this context of increased thermo-mechanical fatigue, the heat-affected zone (HAZ) of welded connections is particularly susceptible to fatigue crack initiation (FCI) [3, 4].

This work focuses on predicting high temperature FCI in P91 steels, which is a key stage of metal fatigue. Traditional models for high temperature fatigue [5-7] do not explicitly incorporate the effects of microstructure, such as grain size, grain boundaries, etc. Existing studies on the nucleation of microcracks have shown that for many materials, microcracks initiate in the slip bands of grains [8, 9]. Although some models, such as Tanaka-Mura [10], have been developed for the effects of microstructure on FCI, these have not generally been applied to materials such as P91 with hierarchical microstructures, due to the complexities of cyclic deformation and associated uncertainty regarding dominant fatigue-critical length-scale. The location of crack initiation depends on microstructure and type of applied stress, among other factors. For high temperature low cycle fatigue (HTLCF) of hierarchical microstructures, the problem is particularly complex due to concomitant temperature-induced microstructure evolution and fatigue damage accumulation.

Tanaka and Mura [10] created an energy balance of the dislocation structure along the persistent slip bands (PSB) to predict crack initiation. For the number of cycles to fatigue crack initiation in a PSB, a closed-form solution was derived, which was expressed in a Coffin-Manson form and shows a Hall-Petch-type dependency on grain size. Chan [11] extended the Tanaka–Mura model to deal with crack initiation along the slip bands, inclusions and notches, and then extended this further to include crack size and related microstructural parameters. Wu [12] revisited the Tanaka–Mura model and, based on the true strain definition, a new fatigue crack nucleation life expression was obtained and validated against (limited) experimental data

on a small number of materials.

Li et al. [13] adopted a dislocation model to study the effects of alloy chemistry, thermal–mechanical treatment and temperature on the tensile deformation process in P91 and P92. Barrett et al. proposed a dislocation mechanics cyclic viscoplasticity model, which combines the key physical and microscopic mechanisms of strengthening and softening at high temperature, which can be applied to predict the cyclic behavior of P91 steel in order to study the effect of microstructure on fatigue crack initiation [14]. More recently, the latter proposed a physically-based high temperature yield strength model for P91 steels which includes the interdependent effects of dislocations, solutes, precipitates and grain boundaries [15]. The fatigue behavior and microstructure evolution of other 9-12% Cr steels have also been studied in detail [16-20].

Hence, a mechanistic-based computational method for predicting high-temperature FCI in P91 steels is developed in the present paper. The method is based on a modified Tanaka-Mura (T-M) [10] model for cyclically-softening behavior, implemented within a physically-based (PB) constitutive framework consisting of high temperature yield strength (YS) and PB cyclic viscoplasticity (VP) models, Chaboche-type viscoplasticity model [21-24]. This will facilitate PB FCI prediction of welded joints for high flexibility, high efficiency power generation. A PB FCI model is presented, which captures material property inhomogeneity in P91 cross-weld (CW) specimen. The model incorporates measured microstructural parameters across HAZ obtained from various published and in-house sources for to estimate YS of P91 parent material (PM), inter-critical heat affected zone (ICHAZ), fine grain heat affected zone (FGHAZ) and coarse grain heat affected zone (CGHAZ). Very little work has been done in modelling the mechanical properties of P91 HAZs, particularly with application to fatigue life prediction. A three-material model was developed by Li [25] to simulate the mismatch of cyclic plasticity in the three different welded regions (PM, HAZ and weld material (WM)) based on the work of Farragher et al [26]. However, the HAZ was treated as a homogeneous material in their work, which omitted key aspects such as HAZ sub-regions and their heterogeneous material properties. During welding, the temperature is high enough to cause transformation to the part to a different microstructure [27]. It is confirmed that significant variation in yield strengths [28] and hardness [29, 30] can be found among various microstructural zones, which is critical for predicting fatigue life of HAZ. Therefore, incorporation of each sub-region of P91 welded joints is necessary for the development of more accurate computational models. Some experimental methods for study the heterogeneity of material properties of P91 welded

joints have been proposed. For example, through the creep tests of Hyde et al. [31], the material data for the HAZs can be obtained, and by the digital image correlation (DIC) tests of Touboul et al. [32], the mechanical response of each zone of P91 welded joint are determined, and the validated constitutive parameters also show that the heterogeneity of the welded joint need to be considered. However, additional experimental work is required for different temperatures and test strain-ranges. In contrast, the approach of the present paper represents, via calibration and validation against HTLCF test data for parent metal and cross-weld tests, of a more accurate FCI prediction model by application of the PB YS and VP models to calibration of five-material cross-weld HTLCF model with the modified T-M model to account for cyclic softening. The method is shown to successfully capture the detrimental effect of welding on HTLCF life and failure of such complex steels.

In the present paper, a physically-based computational methodology for prediction of high temperature fatigue crack initiation in 9Cr steels is developed. Section 2 presents the physically-based yield strength model, physically-based cyclic viscoplasticity model, modified Tanaka-Mura model and five-material finite element model for P91 cross weld specimen. Section 3 presents material parameter identification, investigation of the yield strength heterogeneity and inhomogeneity of the cyclic response across the heat affected zone regions, as well as fatigue crack initiation prediction. The objective is to predict the effect of welding on fatigue crack initiation of P91 welded joint under HTLCF conditions, with a view to gain insight into potential failure locations. Some comparison are made between the predicted behavior and experimental data in Section 4, the Discussion section.

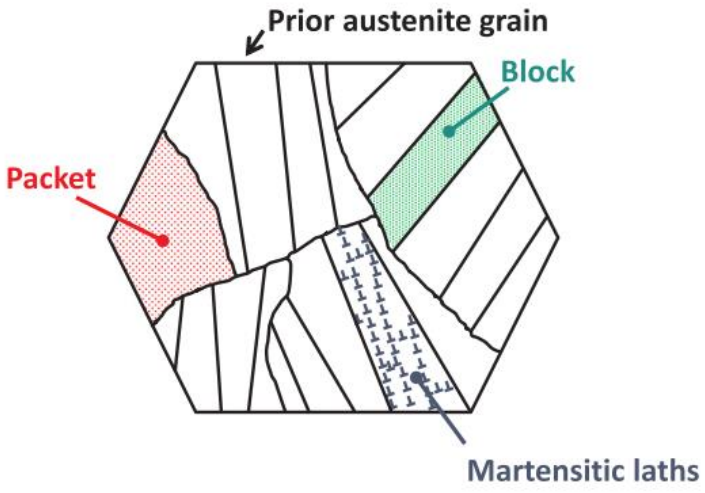

Fig. 1. Hierarchical microstructure of P91 steel [15].

Table 1. Chemical composition of P91 steel in wt. %. The balance is Fe [33, 34].

C	Mn	P	S	Si	Cr
0.08-0.12	0.30-0.60	0.02 max	0.01 max	0.20-0.50	8.00-9.50
Mo	**Ni**	**V**	**Nb**	**N**	**Al**
0.85-1.05	0.4 max	0.18-0.25	0.03-0.10	0.03-0.07	0.04 max

2. Methodology

2.1 Material

In this work, attention is focused on P91 steel weldments. The chemical composition for P91 is presented in Table 1, and the balance is made up of Fe. P91 is a high strength martensitic-ferritic steel, with a complex hierarchical microstructure in nature, consisting of prior austenite grains, packets, blocks and martensitic lath [14], as illustrated in Fig. 1. P91 requires heat treatment (normalizing and tempering) to achieve the desired microstructure and mechanical properties, specifically the required martensitic structure [33, 34], which confers high temperature creep resistance. Also, $M_{23}C_6$ (M = Cr, Fe, Mo, W) carbides are dispersed along grain and lath boundaries and MX (M = Nb, V; X = C, N) carbonitrides within the martensitic lath interiors, which prevent dislocation motion, and further improve creep strength.

In order to identify, calibrate and validate the constitutive and failure models across the heat-affected sub-zones and in the WM and PM, tests results from Farragher et al. [26] are employed, including HTLCF testing of PM, WM and CW specimens obtained from a P91 pipe weldment. The HTLCF tests were conducted at different temperatures, strain-ranges, under isothermal conditions of controlled strain-rate. The results of Farragher's HTLCF tests [26] were analyzed to determine the material parameters of different welding zones.

2.2 Material model

2.2.1 Physically-based yield strength model

Barrett et al. [15] recently presented a temperature-independent, physically-based yield strength model for P91. In the present work, this model is adopted to represent the welding-induced heterogeneity of YS in the different HAZ sub-regions, viz. IC-, FG-, CG-HAZ. This heterogeneity is considered key to capturing the effects of thermal transformations due to

welding on fatigue crack nucleation. The model assumes that the yield strength is composed of contributions from dislocations, τ_{A}, and obstacles, τ_{B}, following the model of Kocks et al. [35], as follows:

$$\sigma_{\mathrm{y}} = M(\tau_{\mathrm{A}}^2 + \tau_{\mathrm{B}}^2)^{1/2} \tag{1}$$

where M is the Taylor factor. τ_{A} is defined by the Taylor hardening expression:

$$\tau_{\mathrm{A}} = \alpha_1 \mu b \sqrt{\rho_{\mathrm{i}}} \tag{2}$$

where α_1 is a material constant between 0.2 and 0.5, μ is temperature dependent shear modulus, b is magnitude of Burgers vector and ρ_{i} is initial dislocation density, whist τ_{B} is defined as the sum of various obstacle contributions:

$$\tau_{\mathrm{B}} = \tau_{\mathrm{PN}} + \tau_{\mathrm{bd}} + \tau_{\mathrm{SS}} + \tau_{\mathrm{in}} + \tau_{\mathrm{ph}} \tag{3}$$

where τ_{PN} is Peierls-Nabarro [36] stress, τ_{bd} is contribution of GBs, τ_{SS} is solute atoms term, τ_{in} is interstitial atoms term and τ_{ph} is precipitates term.

2.2.2 Physically-based cyclic viscoplasticity model

It is well known that the high-temperature 9Cr martensitic-ferritic steels undergo softening during high temperature cyclic deformation [37], due to significant thermo-mechanically induced microstructural evolution. This is attributable to thermomechanical deformation induced microstructure evolution, including specifically reduced dislocation density due to dislocation annihilation and martensitic lath widening [15]. The PB cyclic viscoplasticity model of Barrett et al. [14] based on a dislocation-mechanics framework was specifically developed to represent this complex nano-, micro-scale behavior for macro-scale simulations. This model is adopted here to facilitate interrogation of the effects of differences in cyclically-induced microstructure evolution across the HAZ sub-regions of P91 weldments on HTLCF. The inelastic strain-rate is defined as a function of the key microstructural variables:

$$\dot{\varepsilon}_{\mathrm{in}} = f(d_{\mathrm{b}}, w, \lambda, c, \rho) \tag{4}$$

where d_{b} is martensitic block width, w is lath width, λ is precipitate spacing, c is concentration of solutes and ρ is dislocation density. More specifically:

$$\dot{\varepsilon}_{\mathrm{in}} = A\exp\left(\frac{-\Delta F}{k_{\mathrm{B}}T}\right)\sinh\left(\frac{\sigma_{\mathrm{v}}\Delta V}{Mk_{\mathrm{B}}T}\right)\mathrm{sgn}(\sigma - \sigma_{\mathrm{b}}) \tag{5}$$

where A is the pre-exponential viscous constant, ΔF is the Helmholtz free energy, k_B is Boltzmann's constant, T is the absolute temperature, ΔV is the activation volume, σ_v is viscous stress, σ is stress, σ_b is the kinematic back-stress. The viscous (thermal) stress under uniaxial loading is defined as:

$$\sigma_v = |\sigma - \sigma_b| - \sigma_y^{cyc} \tag{6}$$

where σ_y^{cyc} is cyclic yield stress and kinematic back-stress is:

$$\sigma_b = \sigma_p + \sigma_g + \sigma_w \tag{7}$$

where σ_p, σ_g and σ_w are the back-stress contributions due to particles, dislocation pileups at HAGBs, and dislocation substructure, respectively.

Further details of the original implementation of this model are given in Barrett et al. [14]. A key novelty of the present work is the application of this model, in conjunction with the PB YS model of Section 2.2.1, to the different sub-regions of the HAZ in P91, using physically-measured microstructure parameters from the HAZ sub-regions.

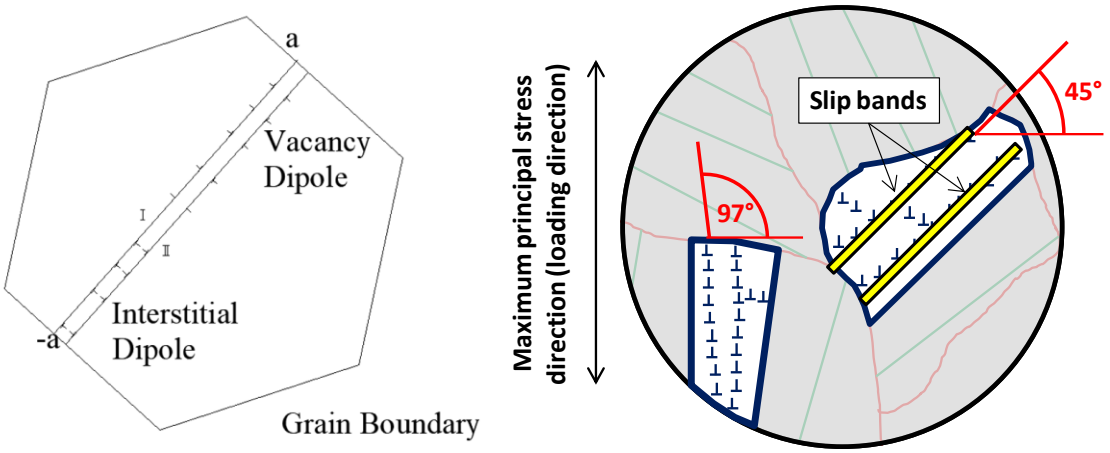

(a) (b)

Fig. 2. (a) Dislocation motion in a grain, adapted from Tanaka and Mura [10], (b) illustration of fatigue persistent slip bands assumed to correspond to packet size in hierarchical microstructure of P91 steels.

2.2.3 Modified Tanaka-Mura model

Tanaka and Mura [10] presented a micromechanical fatigue nucleation model in which dislocations accumulate irreversibly on the slip band of grains, leading to an energy-based crack initiation criterion. The key challenge here is to adapt the Tanaka-Mura model to study

the cyclic softening behaviour of 9Cr steels [37]. The energy-based formulation of Tanaka-Mura is specifically appropriate and suitable for such cyclically-induced microstructure and dislocation evolution, as compared to more commonly-used stress-based approaches. Fig. 2(a) shows the dislocation motion in a favourably oriented grain, of size $2a$. Fig. 2(b) shows the assumed mechanistic basis for fatigue persistent slip bands corresponding to packet size in the P91 microstructure.

The Tanaka-Mura model assumes that if the stored strain energy due to dislocation accumulation becomes equal to a critical value of surface energy after N cycles, the layers of dislocation dipoles transform into a free surface, i.e. a micro-crack. The life to crack initiation N_i is thereby defined as the number of cycles when the following energy condition is satisfied.

$$\begin{cases} \Delta\tau = \dfrac{\Delta\sigma}{M} \\ \Delta\gamma = \dfrac{\Delta\varepsilon^{\mathrm{pl}}}{M} \\ \Delta U = \dfrac{\Delta\gamma(\Delta\tau - 2k)}{2} \\ U \geq 2d_\mathrm{p}w_\mathrm{s} \end{cases} \tag{8}$$

where $\Delta\tau$ is the shear stress range, $\Delta\sigma$ is the stress range ($\Delta\sigma = \sigma_{\max} - \sigma_{\min}$), $\Delta\gamma$ is the shear plastic strain range, $\Delta\varepsilon^{\mathrm{pl}}$ is the plastic strain range ($\Delta\varepsilon^{\mathrm{pl}} = \varepsilon^{\mathrm{pl}}_{\max} - \varepsilon^{\mathrm{pl}}_{\min}$), M is the Taylor factor (taken here as 2.9, based on bcc ferritic-martenstic P91 material), U is the stored strain energy, d_p is the packet size, k is frictional shear stress and w_s is the specific fracture energy per unit area. The key adaptation to the Tanaka-Mura equations here is the use of a combined shear stress-strain ΔU expression within a cumulative computation of U to capture the cyclically-evolving response, due to microstructure evolution effects (e.g. lath coarsening, dislocation annihilation).

2.3 Finite element model of P91 cross-weld

Fig. 3 shows the P91 cross-weld HTLCF specimen of Farragher et al. [26] and the corresponding axisymmetric five-material finite element model developed here, showing the key dimensions identified for HAZ sub-regions. The overall height of the model is 12.5 mm corresponding to the gage length of the extensometer used by Farragher et al. [26]. The width of the HAZ is estimated to be 2.7 mm, as identified from optical microscopy and hardness measurements [26, 38]. Accurate demarcation of the HAZ sub-regions is challenging. Other

authors have similarly attempted detailed SEM measurement of HAZ sub-regions [26, 38], identifying respective widths of 0.7 mm, 0.7 mm and 0.3 mm for IC-, FG- and CG-HAZ respectively. Based on interrogation of the microscopy and hardness data from Farragher et al., in comparison also with the latter (more detailed) measurements, widths of 1.1 mm, 1.1 mm and 0.5 mm are identified here for the IC-, FG- and CG-HAZ regions, respectively.

The yield surface is defined by:

$$f = J(\boldsymbol{\sigma}' - \boldsymbol{\chi}') - R - k \tag{9}$$

where f is the multiaxial flow-rule, $\boldsymbol{\sigma}'$ is the deviatoric stress tensor, $\boldsymbol{\chi}'$ is the deviatoric back-stress tensor, R is isotropic stress, k is the cyclic yield stress. Within the Ziegler non-linear kinematic hardening model [39], two kinematic back-stress terms are defined to describe the initial and later strain hardening regions, as following:

$$\dot{\boldsymbol{\chi}}_{\mathrm{i}} = \frac{C_{\mathrm{i}}}{(k+R)}(\boldsymbol{\sigma} - \boldsymbol{\chi})\dot{p} - \gamma_{\mathrm{i}}\boldsymbol{\chi}_{\mathrm{i}}\dot{p} \tag{10}$$

$$\dot{\boldsymbol{\chi}} = \dot{\boldsymbol{\chi}}_1 + \dot{\boldsymbol{\chi}}_2 \tag{11}$$

The Chaboche isotropic hardening model [23, 24] is used to simulate the measured cyclic softening response of P91, as follows:

$$\dot{R}(p) = b(Q - R)\dot{p} \tag{12}$$

where Q is the saturation value and b controls rate of decay. Cyclic softening is achieved using a negative Q-value [40]. The creep strain is obtained from the multiaxial version of the following Norton power law [41]:

$$\dot{\varepsilon}_{\mathrm{c}} = A\sigma^{\mathrm{n}} \tag{13}$$

where A and n are temperature-dependent material constants, $\dot{\varepsilon}_{\mathrm{c}}$ is creep strain rate. For the five-material cross-weld simulations in Abaqus, the combined NLKIH Chaboche and Norton secondary creep models are used within the two-layer viscoplasticity material model. A two-layer parameter F needs to be defined for each material zone.

The HTLCF cyclic PM and WM behavior was experimentally measured using PM and WM HTLCF specimens machined from the welded connection by Farragher et al. [26]. As discussed in the next section, the NLKIH parameters for IC-, FG- and CG-HAZ regions are identified using the physically-based YS and VP models described above. It is not generally possible to measure this response for these HAZ sub-regions, due to the very small size scale, relative to typical LCF specimen dimensions. A detailed mesh convergence study was

conducted for the five-material model to establish a suitable mesh, with particular focus on the interfaces between the five different weld-affected zones, where material discontinuities occur. The final mesh (shown in Fig. 3) uses an element size (axial direction) of 98 μm, converged to within 5% with respect to maximum principal stress, using eight-node biquadratic axisymmetric quadrilateral elements with reduced integration.

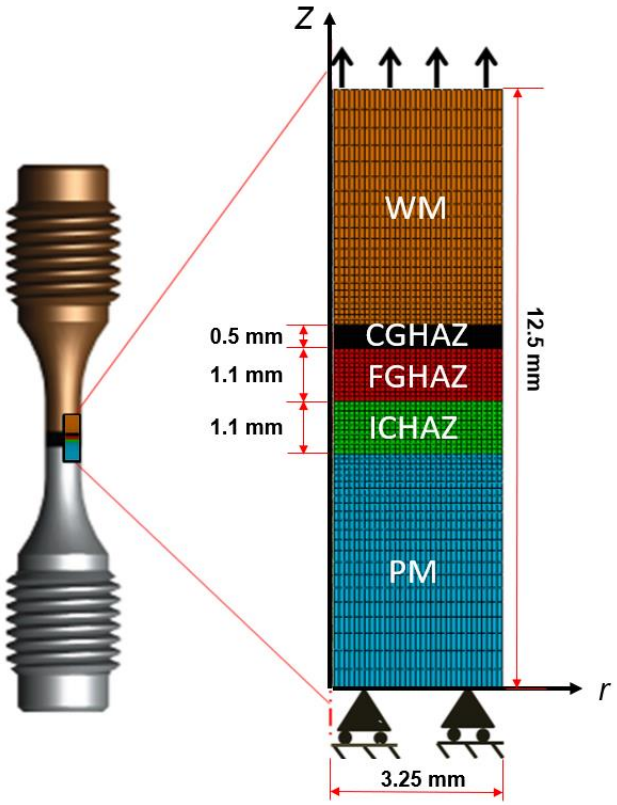

Fig. 3. Schematic of P91 cross-weld HTLCF specimen of Farragher et al. [26] and corresponding axisymmetric five-material finite element model developed here, showing key dimensions for HAZ sub-regions.

3. Results

3. 1 Parameter identification

Representative values for the microstructural parameters required for the proposed physically-based models described above are identified based on previously measured data as summarized in Table 2**,** corresponding to P91 welded joints from published sources [28, 42-44]. In materials with hierarchical microstructure, dislocation density has a strong correlation with lath width. Therefore, the following empirical relationship is used to estimate dislocation density from lath width, based on published data [43, 45-48], as shown in Fig. 4:

$$w^{-1} = 0.161\rho^{1/2} + 11 \quad (14)$$

where w is lath width, ρ is the dislocation density.

Table 2. Identified microstructural parameters for PM, IC-, FG- and CG-HAZ at 500ºC.

Parameter		**PM**	**ICHAZ**	**FGHAZ**	**CGHAZ**
PAG size (μm)		14	18	5	50
d_p (packet size) (μm)		7.6	9.2	4	22
block width (μm)		4	5.3	3	9.1
w (lath width) (nm)		700	600	900	350
ρ_i (mm^{-2})		0.78×10^8	1.06×10^8	0.47×10^8	3.13×10^8
Volume fraction (-)	$M_{23}C_6$	2%			
	MX	0.1%			
radii of precipitates (nm)	$M_{23}C_6$	74	64	100	50
	MX	25	32.5	50	25

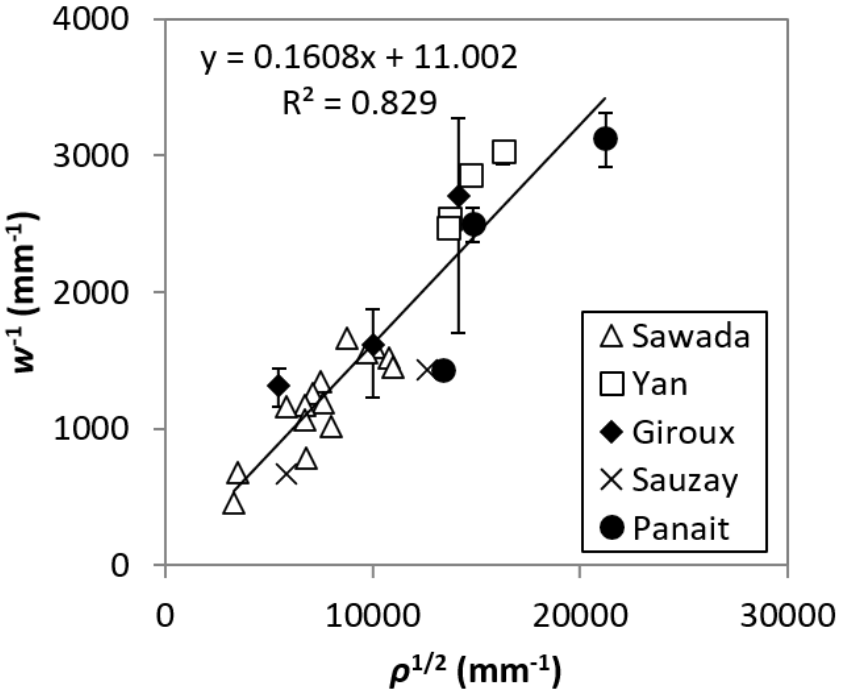

Fig. 4. Relationship between lath width and dislocation density for 9Cr steels based on previously measured data.

Fig. 5 shows the full complex interaction and calibration-identification processes required to combine the different physically-based (PB-YS and PB-VP) and Chaboche NLKIH model with the modified T-M FCI model and the five-material cross-weld HTLCF FE model.

The material parameter identification process (e.g. Barrett et al. [49]) for cyclic NLKIH parameters is applied here to IC-, FG-, CG-HAZ sub-zones, based on the predictions from the physically-based viscoplasticity model for ICHAZ, FGHAZ and CGHAZ. Previously-published material parameters for the PM and WM are adopted here [25]. As shown in Fig. 5(a), Young's modulus, E, and Poisson's ratio, v, are identified first. The isotropic softening constants (Q, b) and kinematic hardening constants (C_i, γ_i) are then identified using a step-by step approach.

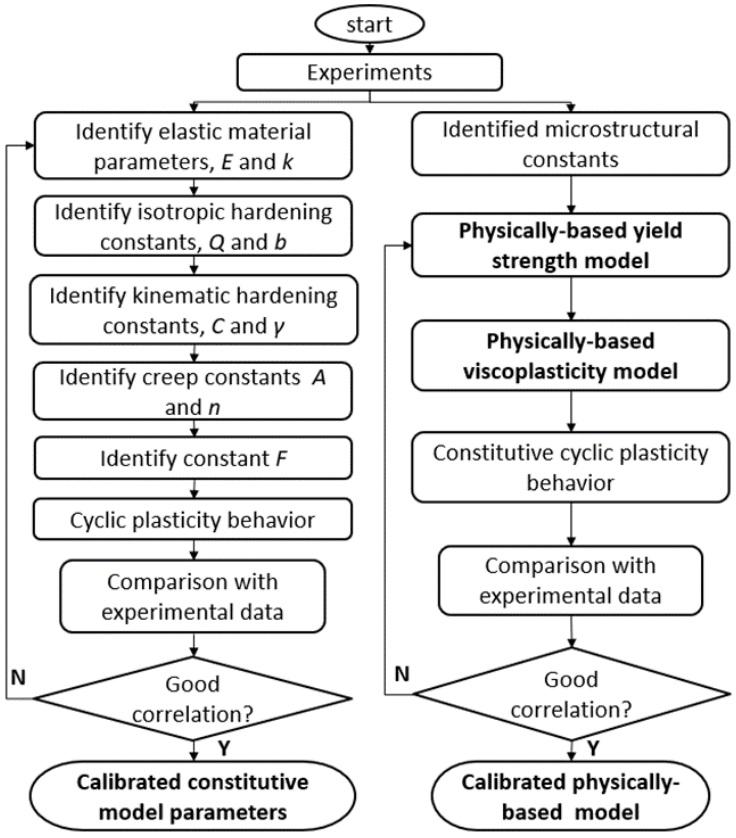

(a) Step 1

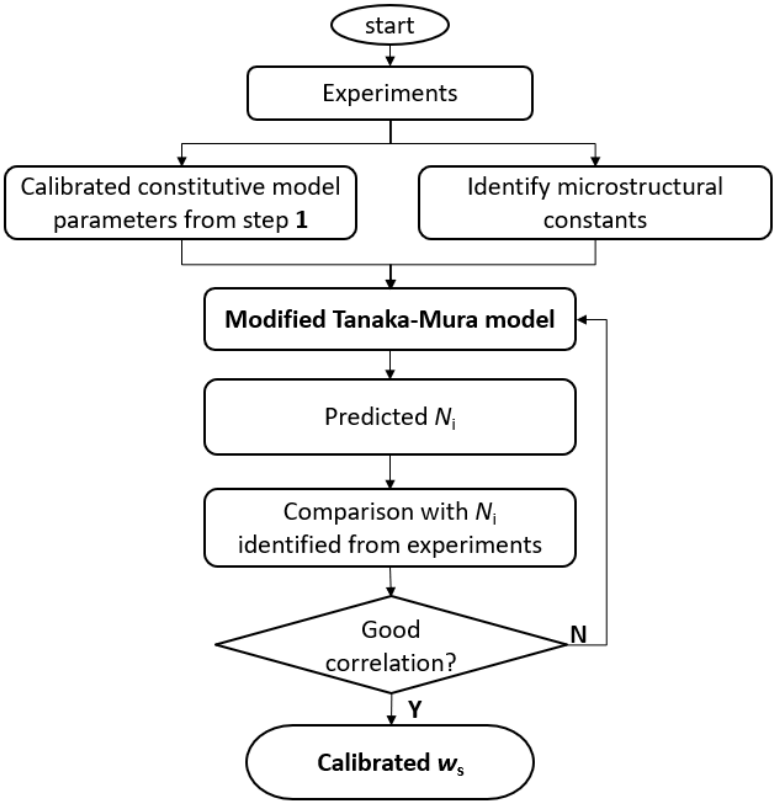

(b) Step 2

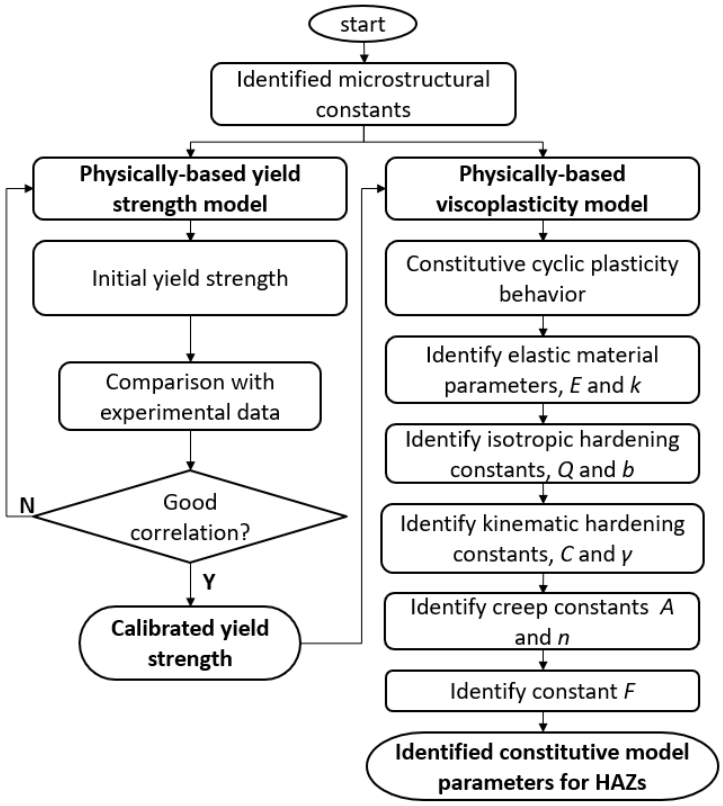

(c) Step 3

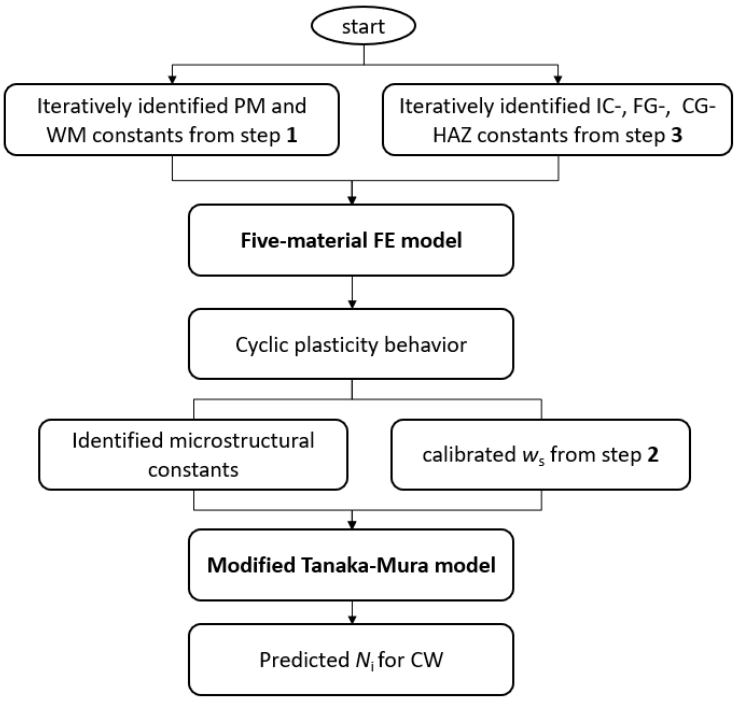

(d) Step 4

Fig. 5**.** Flowchart of main processes for predicting FCI in P91 steels: (a) Step 1: Chaboche NLKIH parameter identification for PM and WM, and calibration of PB model, (b) Step 2: Modified T-M calibration for PM, (c) Step 3: Calibration of Chaboche NLKIH and Norton creep models using PB-YS and PB-VP models for IC-, FG-, CG-HAZ and (d) Step 4: five-material FE model with modified T-M prediction.

The isotropic hardening constants, Q and b, are identified from cyclic softening data derived from the curves of cyclic softening stress and accumulated effective plastic strain. It is assumed in the identification of isotropic hardening parameters that time-dependent microstructure-coarsening effects do not affect isotropic hardening [18]. Under uniaxial loading conditions, the stress is defined as:

$$\sigma = \chi + (R + k + \sigma_{\mathrm{v}})\mathrm{sgn}(\sigma - \chi) \tag{15}$$

The cyclic softening stress R is the difference between the maximum stress of each cycle and that of the first cycle. The accumulated effective plastic strain is estimated for each cycle using the maximum and minimum stresses. The relationship between the accumulated effective plastic strain and a given cycle for LCF is given as below:

$$p = 2\sum_{n=1}^{N}(\Delta\varepsilon - \frac{\Delta\sigma_{\mathrm{n}}}{E}) \tag{16}$$

where N is the total number of cycles where p is obtained, $\Delta\varepsilon$ is the total applied strain range (in a strain-controlled test), and $\Delta\sigma_{\mathrm{n}}$ is the stress range for a given cycle, n. The isotropic softening saturation stress may be estimated when the isotropic softening stress and accumulated effective plastic strain have been obtained. The least squares method is used to fit the b value describing the R decay rate with the experimental data. The b value can be obtained by using the least square method fitting the softening curve with equation (18), as shown for CGHAZ, as an example, in Fig. 6:

$$R = Q(1 - e^{-\mathrm{bp}}) \tag{17}$$

The least squares optimization function to be minimized is:

$$f(b_{\mathrm{k}}) = \sum_{j=1}^{m} (R^{\mathrm{thr}}(b_{\mathrm{k}}) - R^{\mathrm{exp}})^2 \tag{18}$$

where b_{k} represents the material parameters to be optimised and the superscripts 'thr' and 'exp' denote theoretical and experimental values of the cyclic softening stress respectively.

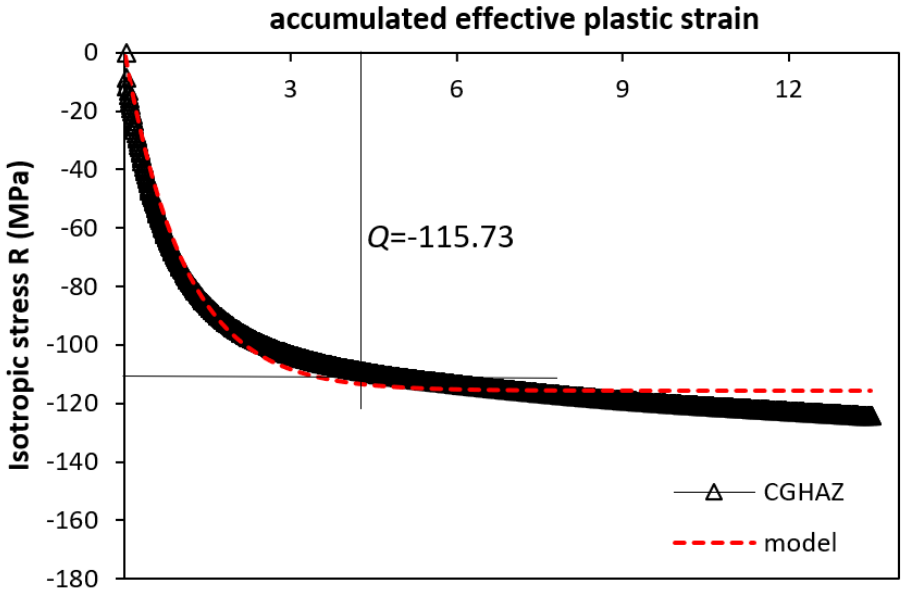

Fig. 6. Softening curve of CGHAZ for 1.0 % strain-range at 500℃.

The non-linear kinematic hardening model is given as:

$$\chi_1 = \frac{C_1}{\gamma_1}(1 - e^{-\gamma_1 \varepsilon_{\mathrm{p}}}) \tag{19}$$

$$\chi_2 = \frac{C_2}{\gamma_2}(1 - e^{-\gamma_2 \varepsilon_p}) \tag{20}$$

It can be assumed that the initial stages of strain hardening (χ_1) have a constant (maximum) value of $\frac{C_1}{\gamma_1}$ when the later stages of hardening are considered. Thus the equation (15) can be simplified to:

$$\sigma = \frac{C_1}{\gamma_1} + \frac{C_2}{\gamma_2}(1 - e^{-\gamma_2 \varepsilon_p}) + R + k + \sigma_v \tag{21}$$

Differentiating equation (21) with respect to ε_p and taking the natural logarithm of both sides to obtain the following equation (assuming yield stress, k, and viscous stress, σ_v, to be constants):

$$\ln\left(\frac{\partial \sigma}{\partial \varepsilon_p} - Qbe^{-bp}\right) = \ln(C_2) - \gamma_2 \varepsilon_p \tag{22}$$

Following the approach of Hyde [50], the term $\frac{\partial \sigma}{\partial \varepsilon_p}$ can be determined using the Ramberg-Osgood equation. The identification of the Ramberg-Osgood parameters for IC-, FG-, CG-HAZ at 500℃ is shown in Fig. 7. Table 3 shows the identified Ramberg-Osgood constants for IC-, FG-, CG-HAZ at 500℃.

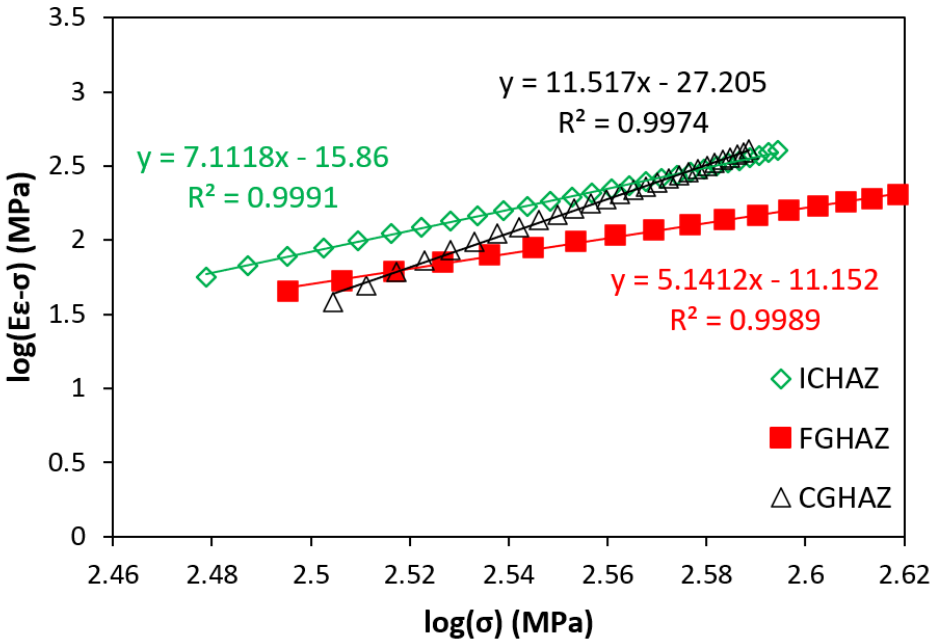

Fig. 7. Identification of Ramberg-Osgood constants for IC-, FG-, CG-HAZ at 500°C.

Table 3. Identified Ramberg-Osgood constants for IC-, FG-, CG-HAZ at 500℃.

Material	σ_0 (MPa)	n_0 (-)
ICHAZ	394.23	7.11
FGHAZ	493.99	5.14
CGHAZ	386.16	11.52

By plotting $\mathrm{In}\left(\frac{\partial\sigma}{\partial\varepsilon_\mathrm{p}} - Qbe^{-\mathrm{bp}}\right)$ versus ε_p , the kinematic back-stress constants C_2 and γ_2 can be determined as intercept and slope, as presented in Fig. 8(a) for CGHAZ, for example. The initial kinematic back-stress term C_1 and γ_1 can then be identified by plotting $\mathrm{In}\left(\frac{\partial\sigma}{\partial\varepsilon_\mathrm{p}} - \frac{\partial\chi}{\partial\varepsilon_\mathrm{p}} - Qbe^{-\mathrm{bp}}\right)$ versus ε_p from equation (23), as presented in Fig. 8(b).

$$\mathrm{In}\left(\frac{\partial\sigma}{\partial\varepsilon_\mathrm{p}} - \frac{\partial\chi}{\partial\varepsilon_\mathrm{p}} - Qbe^{-\mathrm{bp}}\right) = \mathrm{In}(C_1) - \gamma_1\varepsilon_\mathrm{p} \tag{23}$$

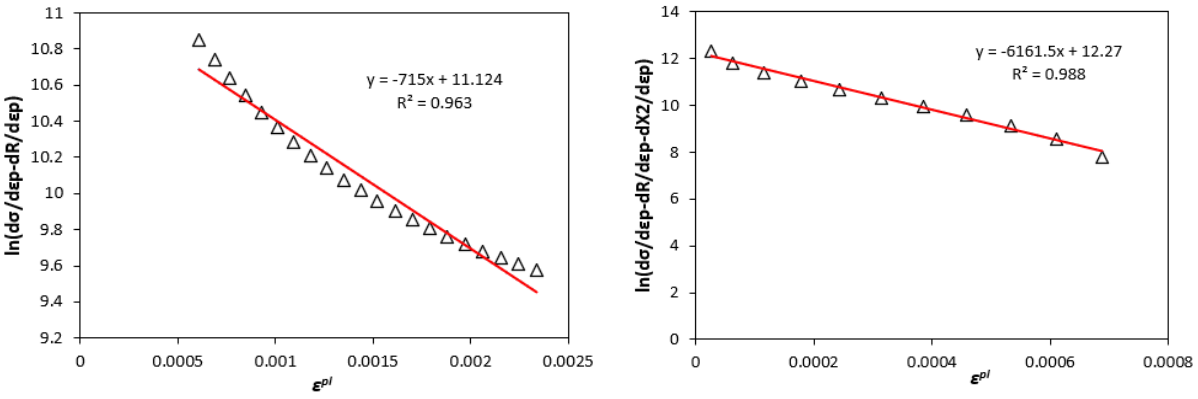

(a) C_2 and γ_2 (b) C_1 and γ_1

Fig. 8. Identification of non-linear kinematic hardening parameters for CGHAZ (a) C_2 and γ_2 and (b) C_1 and γ_1 at temperatures of 500℃.

The same identification process was adopted for ICHAZ and FGHAZ. The final set of identified material parameters for the P91 welded joint are presented in Table 4.

Table 4. Identified cyclic material parameters for PM, IC-, FG-, CG-HAZ, WM at 500℃.

Material	PM	ICHAZ	FGHAZ	CGHAZ	WM
E **(MPa)**	168220	161957	161957	161957	181000
k **(MPa)**	130	125.42	127.24	143.18	325
Q **(MPa)**	-96.5	-57.65	-27.81	-115.73	-150
b	0.25	0.71	0.67	0.92	0.6
C_1 **(MPa)**	728687	257301	362217	213203	797311
γ_1 **(-)**	12534	5459	6358	6162	8035
C_2 **(MPa)**	258073	94278	170416	67778	79567
γ_2 **(-)**	1100	626	727	715	719
$\boldsymbol{A}$ **(MPa^{-n}s^{-1})**	4.28×10^{-40}	2.75×10^{-58}	2.84×10^{-63}	6.76×10^{-57}	1.77×10^{-59}
$\boldsymbol{n}$	13.55	20.84	22.17	20.37	20.2
F	0.1	0.96	0.96	0.96	0.05

The Norton creep constants A and n were identified for each of the IC-, FG- and CG-HAZ regions by calibrating the stress relaxation data as $\log(\dot{\sigma})$ versus $\log(\sigma)$, in comparison with the PB-VP stress-relaxation responses for these sub-zones, with the microstructural data of Table 2. The identified values for each sub-zone are given in Table 4 and comparison of stress relaxation responses predicted by PB-VP model for IC-, FG- and CG-HAZ to the calibrated Norton model responses at 500℃ are shown in Fig. 9(a). Finally, the combined NLKIH-Norton IC-, FG- and CG-HAZ responses, using the two-layer viscoplasticity model in Abaqus, are compared to the stress relaxation responses to identify suitable values of the additional F parameter; the final cyclic viscoplasticity values for all weld-affected sub-regions are given in Table 4. Fig. 9(b) shows a validation comparison of the CW relaxation response from the five-material CW FE model of Fig. 3, using the latter identified parameters for the HAZ sub-regions, with the measured test data at 500^{o}C.

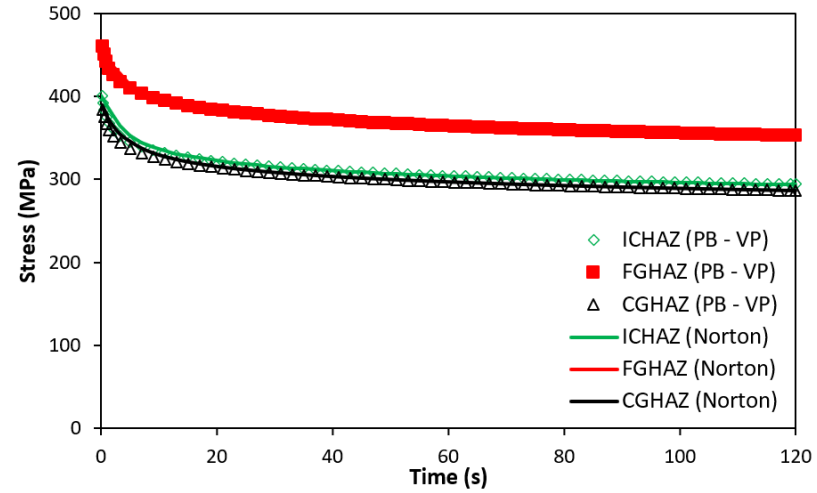

(a)

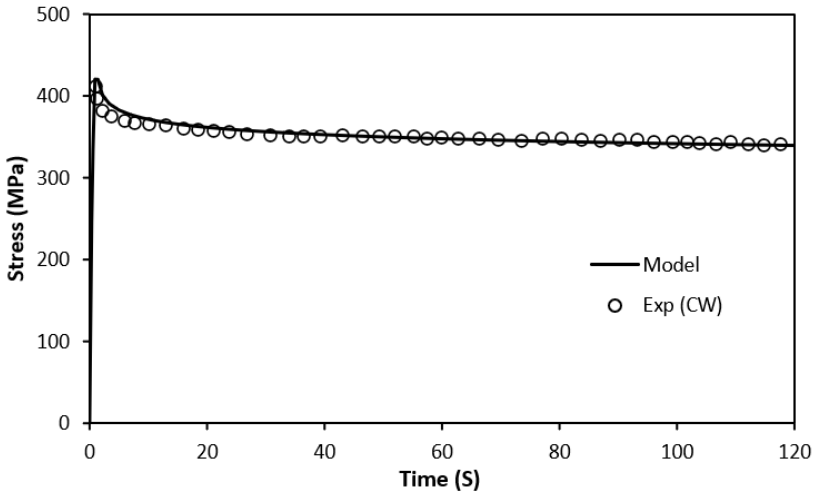

(b)

Fig. 9. (a) Comparison of stress relaxation responses predicted by PB-VP model for IC-, FG- and CG-HAZ to the calibrated Norton model responses at 500ºC (held at 0.5 % tensile strain for 120 s), (b) comparison of FE-predicted (five-material) CW stress response, using calibrated Norton creep constants for HAZ sub-zones, against measured test data for strain-controlled stress relaxation at 500℃.

3. 2 Validation of NLKIH cyclic viscoplasticity model

The predicted constitutive responses of P91 PM, WM and CW are compared with the experimental responses. Details of the experimental methods and results were presented previously [26]. Fig. 10(a) shows the comparison of the predicted and measured responses for PM at 500℃ for strain-range 1.0% and strain-rate 0.033%/s. It is clear that the initial cyclic softening behaviour is captured over the half-life. Fig. 10(b) shows the corresponding softening curves for three different strain-ranges. The effects of fatigue damage on stress response are not included in this work; thus, the final damage-dominated softening, as shown more clearly

in Fig. 10(b), is not explicitly modelled here. Comparisons for the WM are shown in Fig. 11, showing similar level of agreement up to half-life. Fig. 12 shows the predicted response using the five-material FE model of the cross-weld HTLCF tests including comparisons for three strain-ranges. In this case, only 500 cycles are simulated, up to stabilisation of the secondary softening response. The comparisons capture the key trends of the experimental data up to about 500 cycles; similar agreement was obtained for the other strain-ranges, 0.6% and 0.8%.

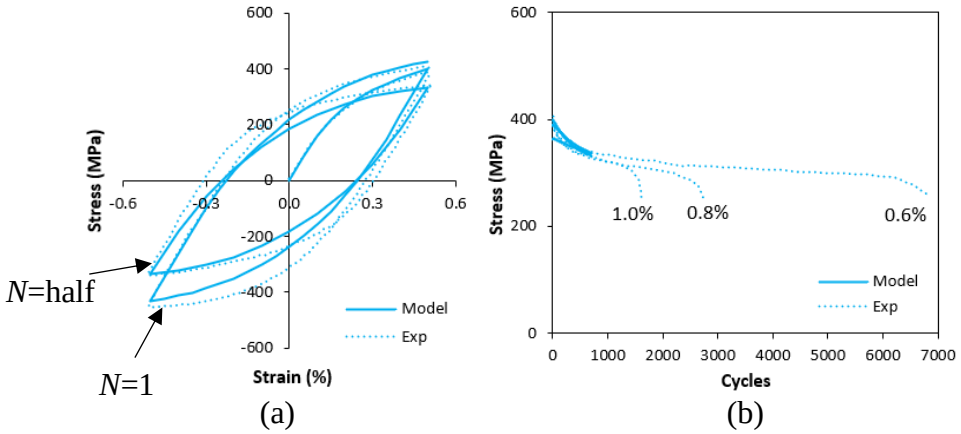

Fig. 10. Comparison of predicted and test observed (a) stress-strain response for 1.0% strain-range at 0.033%/s and (b) cyclic softening in PM at 500℃.

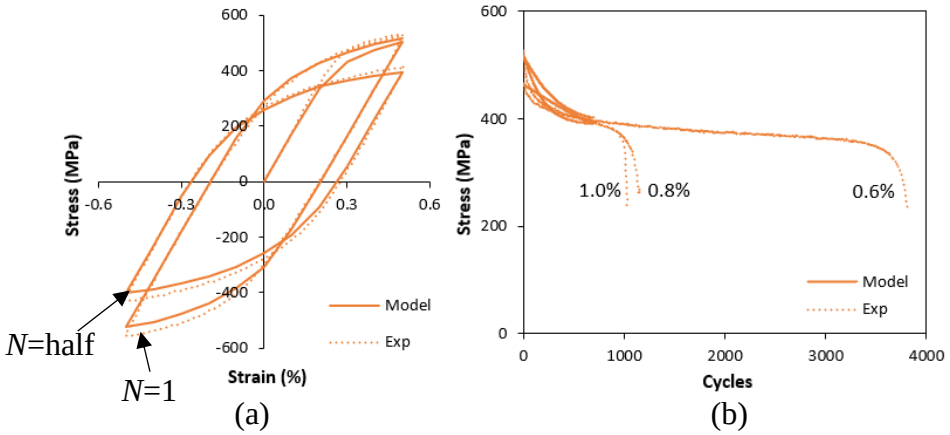

Fig. 11. Comparison of predicted and test observed (a) stress-strain response for 1.0% strain-range at 0.033%/s and (b) cyclic softening in WM at 500℃.

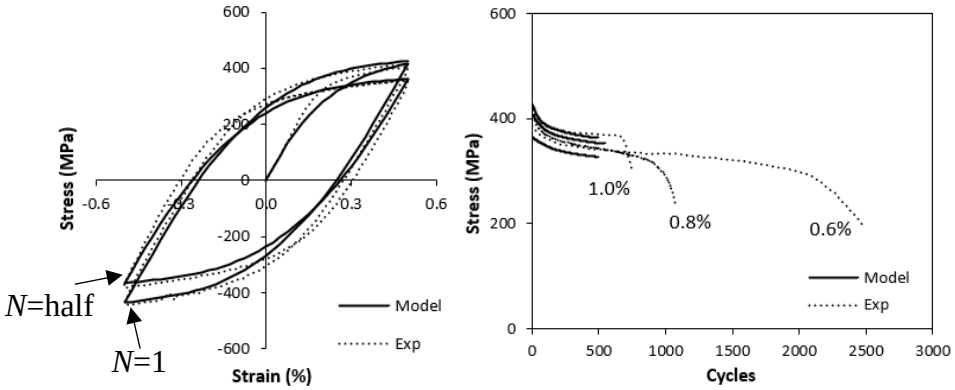

(a) (b)

Fig. 12. Comparison of predicted and test observed (a) stress-strain response for 1.0% strain-range at 0.033%/s and (b) cyclic softening in CW at 500℃.

3. 3 Grain boundary strengthening

As can be seen from Table 2, the grain diameter of CGHAZ is around 10 times that of FGHAZ, and lath width of FGHAZ is highest among these materials, which is approximately 2.5 times that of CGHAZ. Because of the hierarchical microstructure of P91, predicted grain diameter that contributes to grain boundary strengthening is based on the minimum HAGB dimension (mean block width). The calculated grain boundary strengthening contributions are presented in Table 5. The contribution of LAB is significantly larger than that of HAGB, except perhaps for FGHAZ, illustrating the key role of LAB strengthening at high temperature. It is calculated that the total contribution of grain boundaries in FGHAZ is the largest, primarily due to the significant HAGB contribution.

Table 5. Predicted grain boundary YS contributions (MPa).

Boundary	PM	ICHAZ	FGHAZ	CGHAZ
HAGB	17.94	16.84	22.43	12.86
LAB	24.23	24.37	26.39	29.37
Total	42.17	41.21	48.82	42.23

3. 4 Yield strength heterogeneity

Fig. 13 shows the comparison of the contributions from different strengthening mechanisms for P91 welded joints. In all cases, the most significant YS contributor is the Taylor hardening (dislocation), each accounting for 15% and 30% of the total yield stresses;

other main strengthening mechanisms include the Peierls-Nabarro stress, solid solution strengthening HAGB and LAB strengthening and precipitate strengthening. The higher dislocation density of the CGHAZ leads to a significantly higher dislocation strengthening contribution for this sub-zone. Fig. 14 shows (a) the hardness profile of the actual P91 weld joint at 550℃ and (b) a comparison of the calculated yield stresses for P91 welded joint at 500℃. The results of the PB-YS model show the following order of yield strengths of each zone: CGHAZ > PM > FGHAZ > ICHAZ, which is consistent with observed hardness measurements [28, 29, 51]. Compared with FGHAZ, the YS of ICHAZ is lower, mainly due to increased packet size.

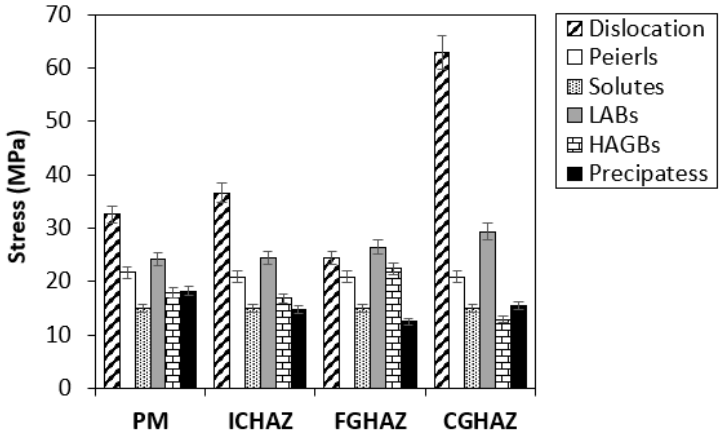

Fig. 13. YS contributions of major strengthening mechanisms for P91 welded joint at 500℃.

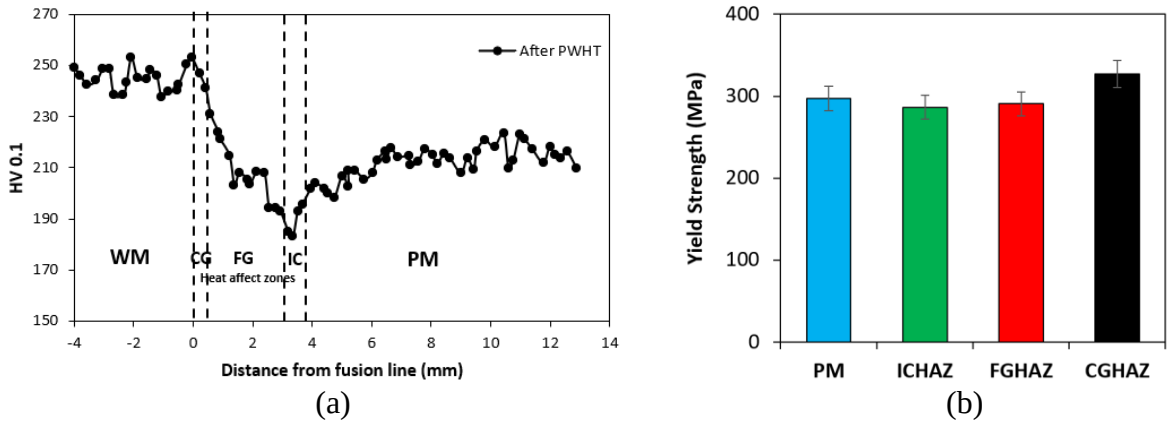

(a) (b)

Fig. 14. (a) Hardness values of P91 weld joint at 550℃ , adapted from [28] and (b) comparison of results of PB YS model at 500℃.

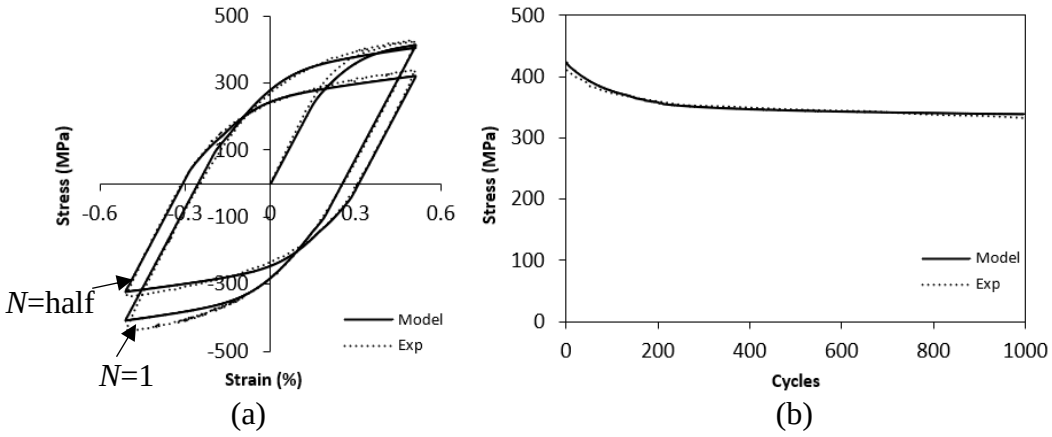

Fig. 15. Comparison of PB-VP model and test data for (a) stress–strain response for 1.0% strain-range and (b) cyclic softening in PM at 500 ℃.

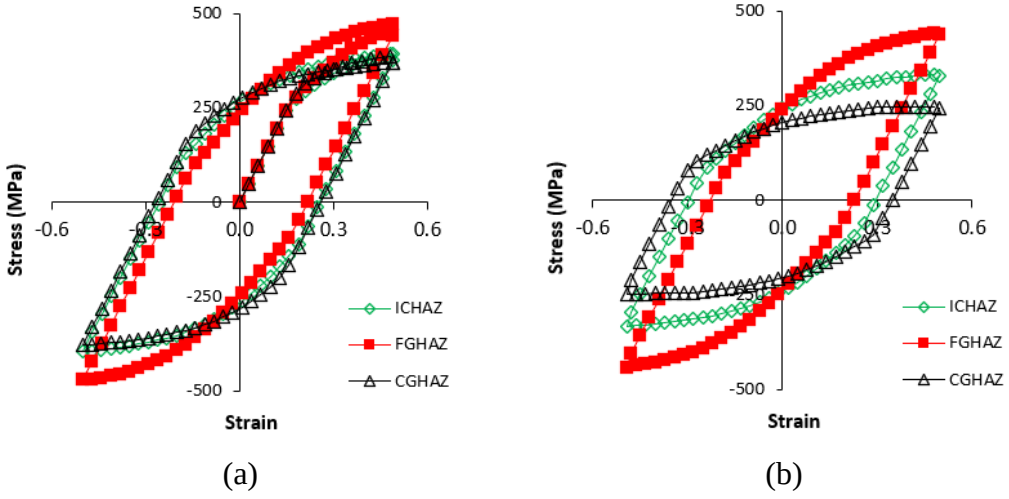

Fig. 16. The predicted stress-strain response for P91 IC-, FG-, CG-HAZ at 500℃ with (a) N=1, (b) N=1000 for 1.0% strain-range.

Fig. 15(a) shows the comparison of PB-VP predicted response against the test data for PM at 500 ℃. The comparison of softening behaviour is shown in Fig. 15(b). Fig. 16 presents the stress-strain responses predicted by the PB-VP model for IC-, FG-, CG-HAZ at the 1st and 1000st cycle for 1.0% strain-range. The model predicts significant differences across HAZ, due to different martensitic block width and lath width for three sub-zones. Compared with ICHAZ and FGHAZ, CGHAZ exhibits the softest response because the block width increases and the lath width decreases significantly. FGHAZ showed the hardest response through the cycles, which is due to the reduced block width and prevalence of lath microstructure, compared with ICHAZ. The comparison of predicted and experimentally measured evolution of cyclic softening in P91 welded joint is shown in Fig. 17. It can be clearly seen that the FGHAZ is significantly harder than the other HAZ sub-zones through all the cycles, and the model

predicts that CGHAZ is the cyclically softest region in the HAZ due to the coarse microstructure. The evolution of strain distributions for the cross-weld five-material model after different numbers of HTLCF cycles are presented in Fig. 18. These results indicate that (i) the inhomogeneity of all five regions (PM, IG-, FG, CG-HAZ and WM) is significant, and (ii) the inhomogeneous distribution of strain in the loading direction evolves from the first cycle due to the heterogeneous material behaviour of HAZ sub-zones. As the number of cycles increases, strain re-distribution occurs throughout the HAZ sub-zones, in particular, leading to significant strain localisation within the CGHAZ near the outer surface.

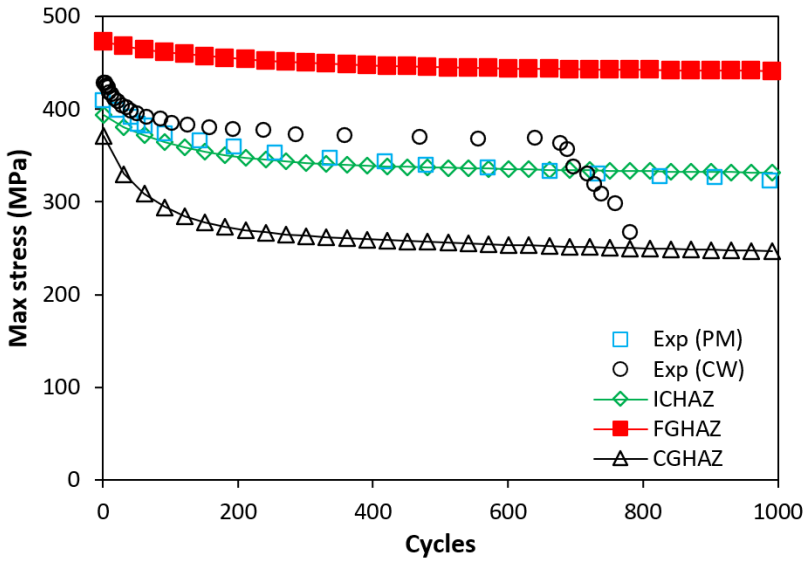

Fig. 17. Comparison of predicted and measured cyclic softening in P91 welded joint for 1.0% strain-range at 500℃.

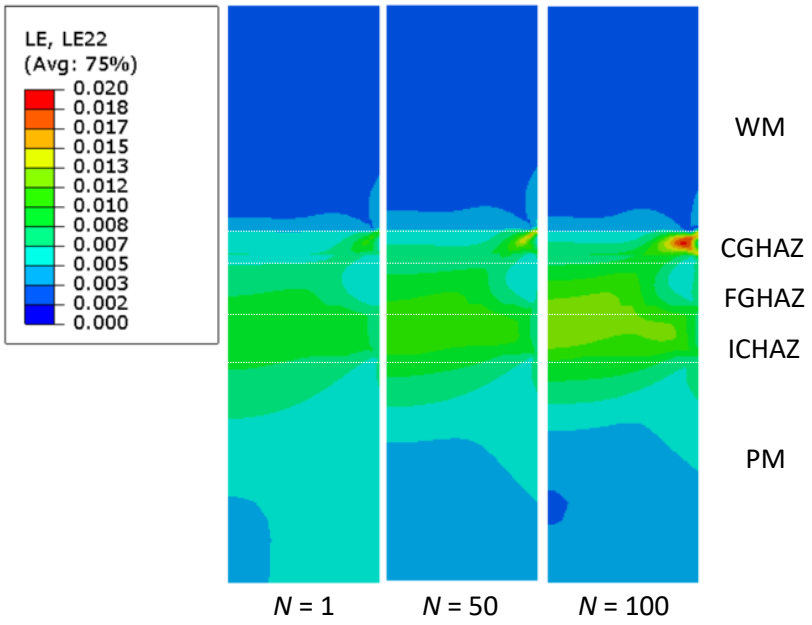

Fig. 18. Cyclic evolution of (axial) strain distribution in the FE model of P91 CW HTLCF cylindrical test specimen for 1.0% strain-range at 500℃.

3.5 Identification of Tanaka-Mura parameters for parent material

A key novelty of the present work is the calibration of the modified Tanaka-Mura model for the cyclically-softening HTLCF behaviour of P91. Fig. 19(a) shows the typical cyclic softening maximum stress evolution with number of cycles for HTLCF testing of PM at 500℃ for $\Delta\varepsilon$ =1.0%. Fig. 19(b) shows the procedure adopted here for identification of FCI for PM tests at 500℃ [26, 52], based on the assumption of initiation being identified with end of the estimated recovery-induced softening phase. Using this approach for the corresponding HTLCF test data at 400℃, 500℃, and 600℃, the Tanaka-Mura critical surface energy w_s values have been identified, as shown in Table 6. Fig. 20 shows the comparison of resulting T-M predictions against the experimental data. In general, the model slightly under-predicts for the lower strain ranges at 400℃ and 500℃, whereas at 600℃ it slightly under-predicts for the higher strain ranges. Overall, reasonably good agreement is obtained between the predictions and experiments. The data in Table 6 shows a significant effect of temperature on critical surface energy.

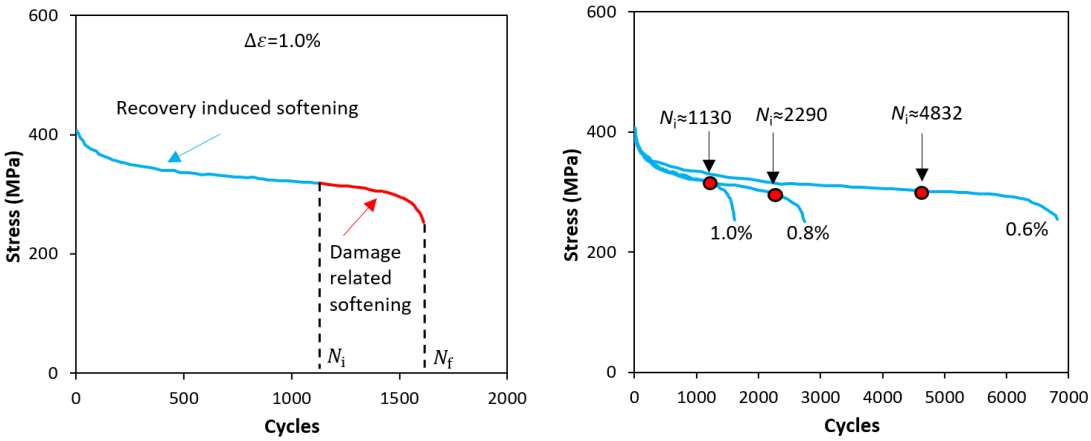

(a) (b)

Fig. 19. (a) Cyclic softening of PM 1.0% strain range at 500 °C, (b) the identification of FCI for PM tests at 500℃.

Table 6. Identified w_s for PM at 400, 500 and 600℃.

T (℃)	w_s (J/m^2)
400	22
500	15
600	7.5

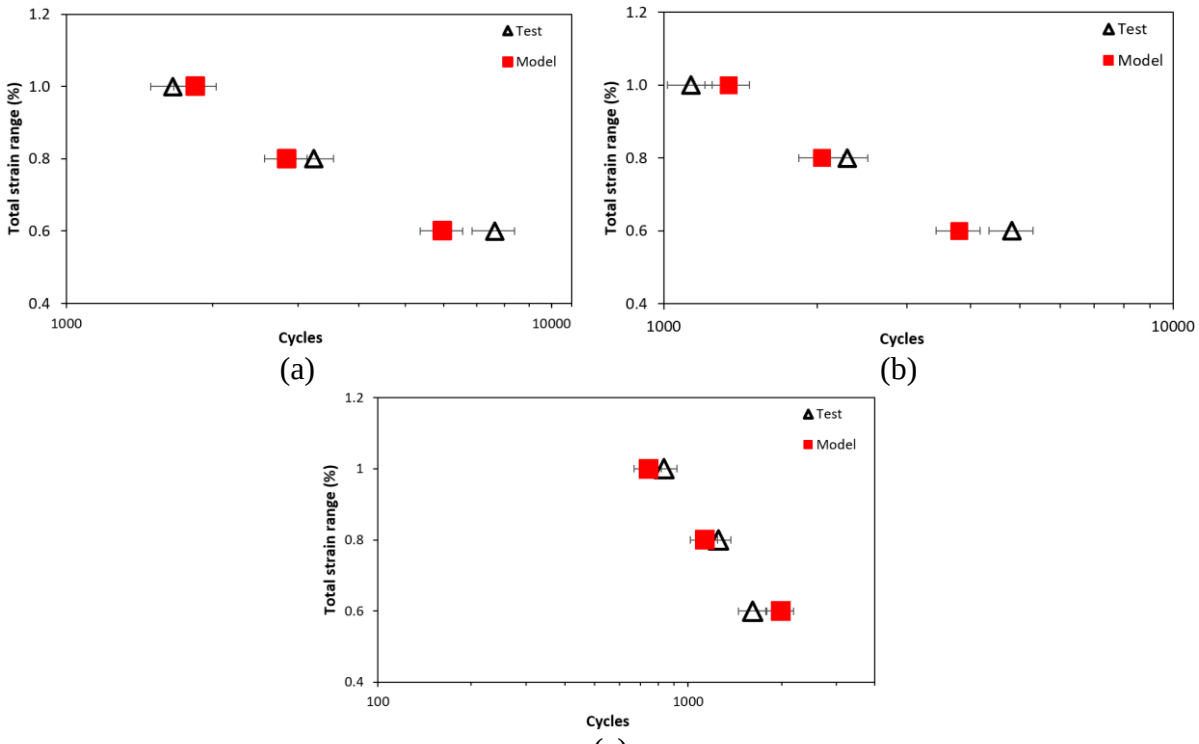

(a) (b)

(c)

Fig. 20. The comparison of FCI prediction to experimental results for PM (a) 400℃, (b) 500℃, (c) 600℃.

3.6 Fatigue crack initiation prediction using modified Tanaka-Mura model for five-material model

The overall end objective of the present work is to facilitate prediction of the effect of welding on fatigue crack initiation. Consequently, the cross-weld (five-material) model, with the NLKIH model calibrated via the physically-based YS and VP models, and combined with the modified T-M model, as shown in Fig. 5, has been applied here for FCI prediction, with comparison against measured HTLCF test data at 500℃. Fig. 22 shows the comparison of FCI predictions for PM and CW under different strain ranges at 500℃, thus conveying the weld strength reduction factor due to welding on HTLCF. The scatter bar is obtained from the standard deviation of packet size, which is the critical length-scale for slip band formation in the modified Tanaka-Mura model. The model slightly under-predicts the effect at the higher and lower strain-ranges. Overall, it is clear that the model successfully captures the significant reduction (knockdown) in FCI life due for the cross-weld P91 HTLCF tests. Fig. 23 shows the predicted FCI of the modified T-M model for the different HAZ sub-zones. The minimum life is predicted in FG-HAZ as 299 cycles and IC-HAZ as 613 cycles, which are significantly lower than for PM (1340 cycles) and CG-HAZ (2051 cycles). Fig. 21 shows the evolution of normalized stored strain energy (energy divided by failure energy of that local region) distributions for the cross-weld five-material model after different numbers of HTLCF cycles. The contour plot shows predicted FCI in the FGHAZ, towards the interface with ICHAZ.

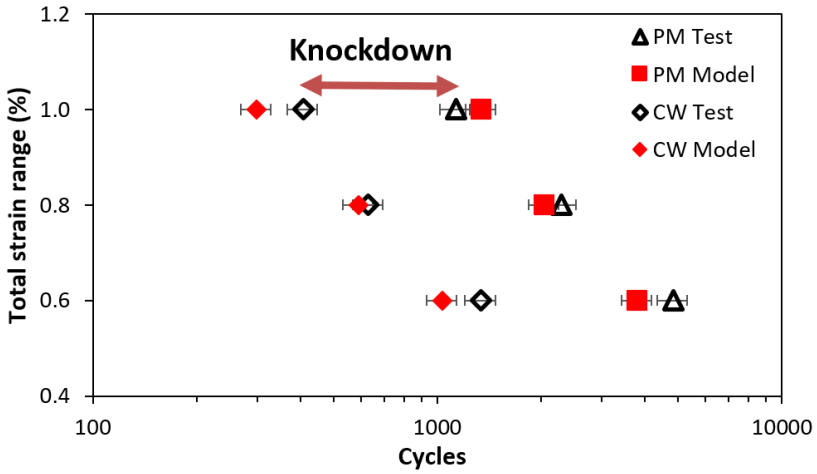

Fig. 22. Comparison of FCI prediction for PM and CW for HTLCF tests at 500℃.

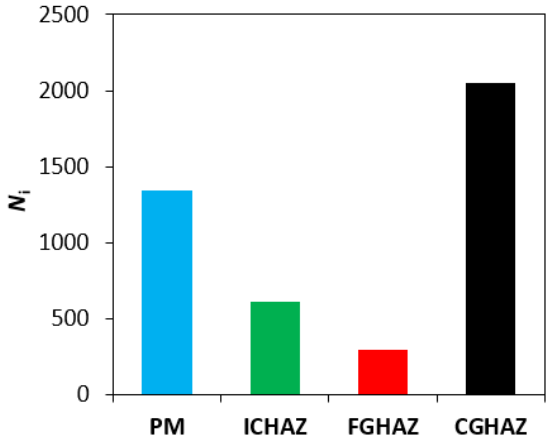

Fig. 23. Comparison of predicted cycles to FCI in different sub-zones of the HAZ using the modified T-M equation and the five-material FE cross-weld model for 1.0% strain range at 500℃.

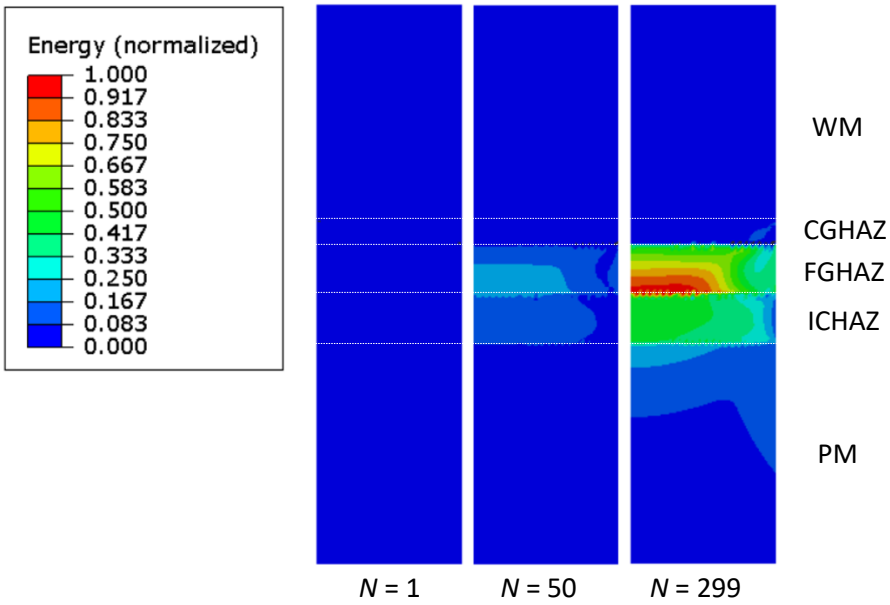

Fig. 24. Cyclic evolution of normalized stored strain energy distribution in the FE model of P91 CW HTLCF cylindrical test specimen for 1.0% strain-range at 500℃.

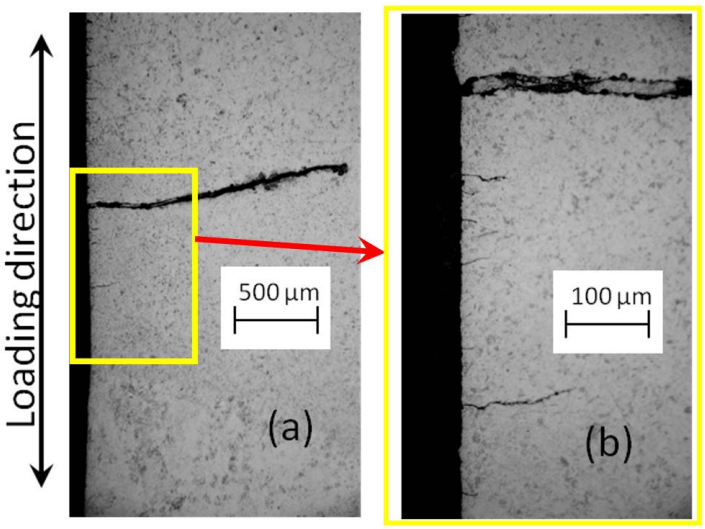

Fig. 25. Optical micrograph of (a) primary crack (occurring in the HAZ) and (b) magnified view of primary and secondary (surface) crack of the CW specimen for 1.0% strain range at 500℃ [26].

4. Discussion

The proposed mechanisms-based computational model shows that IC-, FG-HAZ regions are key hotspots for HTLCF crack initiation in welded P91. The five-material model, calibrated via physically-based YS and viscoplasticity models, with modified Tanaka-Mura, predicts the inhomogeneity in cyclic response between across the HAZ region and detrimental effect of welding on fatigue crack initiation.

The physically-based YS model presented here for weld-affected P91 captures the measured YS inhomogeneity across the P91 welded joint [28, 32]. Specifically, the model captures the increased YS (and thus hardness) value for CGHAZ, about 10% increase for the model compared to about 15% measured, and the decrease for ICHAZ material, about 5% predicted compared to about 10% measured. Mariappan et al. [28] have suggested that the substantial decrease of yield strength from CGHAZ to FGHAZ and ICHAZ is due to the lower soaking temperature during PWHT leads to a decrease in the solubility of MX-type precipitates and hence in solid solution strengthening contribution. Despite the significantly higher HAGB strengthening in FGHAZ, compared with that of CGHAZ, due to grain (mean block width) refinement, the significantly reduced lath width and increased dislocation density lead to pre-dominant dislocation strengthening contribution (Taylor hardening) in the CGHAZ. It can thus be concluded that with measurable microstructural parameters in the different weld-affected material regions, the physically-based YS model can predict welding-induced YS inhomogeneity, both qualitatively and quantitatively, with reasonable accuracy.

The influence of the microstructure and the strain-range on the first and stabilized stress-strain response of P91 welded joint is accurately captured by the physically-based cyclic viscoplasticity model, through the difference between the width of the martensite block and the width of the lath. The results show that the model based on the rule of mixtures formulation is in agreement with the experimental data. Specifically, for example, the maximum stresses have been calculated quite well compared to the measured data [26], and the general shape of the loop is captured. The inhomogeneity of cyclic softening response within the PM and across the different HAZ sub-regions is also captured by the model, consistent with the DIC-measured observations of Touboul et al. [32] for tensile response of P91 welded joints at 625ºC. The physical cause of the increased softening rate in CGHAZ, e.g. see Fig. 16, is the presence of freshly formed martensite combined with new, uncoarsened laths with high dislocation density [53]. The present physically-based model captures cyclic softening via evolution of the low angle boundary microstructure in P91 steels, including precipitate hardening and hierarchical grain boundary strengthening.

A five-material FE model was developed to study the HTLCF behaviour of P91 cross weld test specimens. It is known that long-term and short-term responses of materials like P91 at high temperature differ significantly [54], so that the Norton constants for short-term creep are generally different to those for long-term creep. The two-layer viscoplasticity model has been successfully employed for P91 under HTLCF conditions [22]. Only the short term creep response is directly relevant to this work, since we are looking at HTLCF prediction, not involving long term creep. Fig. 9(b) shows the validation comparison of FE-predicted (five-material model) CW stress relaxation response of the two-layer viscoplasticity model used here, which shows reasonably good correlation with the experimental data. The five-material FE model used here thus captures reasonably well the short-term stress relaxation effect in P91 steels under HTLCF conditions, although more extensive calibration and validation may be required to confirm applicability across a broader range of strain-rate and stress. Focusing on the strain distribution of the entire welded joint, the results show that as the number of cycles increases, complex cyclic evolution of multi-material stress and strain re-distribution is observed due to changes of constitutive behaviour of each material. CGHAZ predicted to have the highest strain concentration after significant cyclic loading. One might expect cyclic strain localization to concentrate within the ICHAZ, due it being the softest weld-affected sub-zone in P91 welded joints. However, the present modelling results demonstrate a more complex trend, viz. since the CGHAZ is determined to display a more rapid and extensive cyclic

softening, strain localization appears there, mainly near the edges of the welded joint. However, this is not pre-dominant in terms of failure location (see Fig. 23). The normalised stored strain energy in Fig. 26 is the ratio of local (integration point) energy to critical Tanaka-Mura energy for crack initiation in that material zone. Hence, a value of 1 for normalised energy indicates Tanaka-Mura fatigue crack initiation (FCI) at that material point. Significantly lower cycles to FCI are predicted for IC- and FG-HAZ than for CG-HAZ, despite the cyclic strain localisation in the latter. This is consistent with the observed cracking of P91 cross-weld HTLCF specimens in Fig. 25, indicating cracking within the FG- and IC-HAZ regions [26].

Table 7. Comparison of measured and predicted weld life reduction factors (WLRF) for HTLCF of CW specimen at 500ºC.

Strain-range (%)	**Test**	**Modified Tanaka-Mura model**
0.6	3.6	3.7
0.8	3.6	3.5
1.0	2.8	4.5

A key novel contribution of this work is the modification of an energy-based Tanaka-Mura (T-M) method to account for cyclic softening in 9Cr steels, with packet size as the critical length scale for slip band formation [18], which is characteristic length in a hierarchical microstructure. The predictions of this mechanisms-based computational model are shown to agree consistently with initiation lives inferred from published test data for the effect of welding on HTLCF life in CW test specimens [26]. The modified T-M model has been adapted to predict cycles to FCI for the P91 welded joint. The results are in qualitative agreement with the findings from Shankar's work at 550ºC and 600ºC [4], which also showed failure within the ICHAZ (also consistent with the present work) and a detrimental effect of welding for HTLCF of P91 CW tests. The phenomenon of continuous cyclic softening here is a complicating factor, in terms of utilising a conventional load-drop approach, for example. In this work, based on the rationale of Li et al. [Li, 2017], the number of cycles to crack initiation has been estimated from the cyclic softening curves for each strain-range and temperature (e.g. see Fig. 19(b)), based on the assumption that the initial cyclic softening (gradual load drop with decreasing rate) is high temperature recovery-induced in terms of dislocation annihilation and microstructure coarsening, leading to diffuse micro-cracking, not due to the presence of a localised macroscale

crack (e.g. as might occur after coalescence of multiple micro-cracks), giving a final, more sudden load drop towards zero, with increasing rate. Hence, in this work we distinguish between cycles to initiated micro-cracking N_{i} (identified as the end of recovery-induced softening in Fig. 19(a)) and macro-scale cracking N_{f}, corresponding to final, more sudden load drop towards zero, with increasing rate. Nonetheless, it is true that slip band crack initiation will be conservative relative, even, to the recovery-induced N_{i}. Table 7 shows a comparison of predicted and measured weld life reduction factors, where $WLRF = N_i^{\mathrm{PM}}/N_i^{\mathrm{CW}}$, is the ratio of numbers of cycles to FCI in PM to that in CW. Clearly, the model and test data both show significant reduction in FCI life due to welding, and very close correlation for lower strain-ranges; the model is conservative relative to the test data at the highest (1%) strain range. Significant WLRF is also predicted by Mac Ardghail for HTLCF [55], with damage initiating in the ICHAZ during welding. Devaney [56] showed that the impact of welding on the room temperature fatigue life performance of X100 bainitic steel is very significant, resulting in a life reduction of up to two orders of magnitude. Long [57] provided a mechanistic explanation for the detrimental effect of welding on fatigue of X100 using FE modelling combined with physically-based modelling. A key next step for welded connections and the present model, is the extension to include fatigue crack propagation. Recently, Kramberger et al. [58] have presented a multi-scale numerical approach for evaluation of fatigue crack initiation and propagation in thermally cut martensitic steels, where the micro-crack initiation in the sub-model is based on the Tanaka-Mura model, similar to the present work, and fatigue crack propagation in the macro model is predicted using linear elastic fracture mechanics (LEFM), showing reasonably good correlation with experimental test results.

In future work, it is planned to combine the current model with a microstructure evolution model, such as the model developed by Mac Ardghail [59].

5. Conclusions

This paper presents a mechanisms-based fatigue crack initiation model for the effect of welding on the high temperature low cycle fatigue of P91 steel. The method is based on the combined use of (i) a modified Tanaka-Mura equation for cyclic softening martensitic steel, due to microstructure evolution effects, including lath coarsening and dislocation annihilation, (ii) application of previously-published physically-based yield strength and cyclic viscoplasticity models to the different material zones in a cross-weld specimen and (iii) implementation within phenomenological finite element modelling of the cross-weld high

temperature low cycle fatigue tests. The key conclusions are:

- The physically-based yield strength model enables prediction of yield strength heterogeneity as a result of welding-induced metallurgical transformations on the P91 welded joints. The measured microstructural parameters of the heat affect zone obtained from published sources provide insights into the changes in the key strengthening mechanisms that lead to yield strength inhomogeneity in P91 steel.
- Variations in block width and lath width are shown to have a significant effect on yield strength heterogeneity. Compared with the coarse grain heat affected zone, the reduced block width in fine grain heat affected zone resulting in an 74% increase in high angle grain boundarie strengthening. The reduction in the lath width causes coarse grain heat affected zone to have the highest low-angle boundary strengthening and the highest Taylor hardening contribution, leading to highest yield strength in the coarse grain heat affected zone.
- The dislocation-mechanics cyclic viscoplasticity model successfully predicts the inhomogeneity in cyclic response across the heat affected zone region by directly representing the microstructural parameters of these different regions, which is also a key step to predict the inhomogeneous constitutive and fatigue life of P91 welded joints. coarse grain heat affected zone is determined to have the highest degree of cyclic softening, and consequently rapidly becomes the cyclically softest heat affected zone sub-zone.
- The constitutive behaviours of different regions of P91 welded joints including parent material, inter-critical heat affected zone, fine grain heat affected zone, coarse grain heat affected zone and weld material have been successfully modelled using a Chaboche-type viscoplasticity model, which have also been used in the five-material FE model. With an increasing cycle number during high temperature low cycle fatigue loading, complex cyclic evolution of multi-material stress and strain re-distribution are observed across the cross weld fatigue model; coarse grain heat affected zone is predicted to have highest cyclic strain localisation.
- A modified form of the energy-based Tanaka-Mura equation has been developed for cyclically-softening metal and applied to successfully predict effect of strain-range on high temperature low cycle fatigue crack initiation in cyclic softening 9Cr steel at different temperatures.
- The modified Tanaka-Mura model has been applied to the different weld-affected sub-

zones, including inter-critical , fine grain and coarse grain heat affected zone , as well as parent material and weld material, on the basis of packet size the key microstructural length scale for crack initiation, to successfully predict (i) the detrimental effect of welding and (ii) the quantitative effect in terms of weld life reduction factor. The inter-critical and fine grain heat affected zone regions are predicted as key hotspots for fatigue crack initiation in high temperature low cycle fatigue, consistent with previously published experimental work.

- Dislocations, precipitates, solutes, and high and low angle grain boundaries strengthen the complex hierarchical microstructure of 9Cr steels. It is necessary to establish a physical-based yield strength model, combined with physically-based strengthening and softening mechanisms and life prediction method, to accurately explain the microstructure evolution caused by the interaction of creep, fatigue and oxidation.

Acknowledgements

This publication has emanated from research conducted with the financial support of Science Foundation Ireland under Grant number SFI/14/IA/2604 and SFI/16/RC/3872. For the purpose of Open Access, the author has applied a CC BY public copyright licence to any Author Accepted Manuscript version arising from this submission.

References

[1] T.P. Farragher, S. Scully, N. O'Dowd, S. Leen, Thermomechanical analysis of a pressurized pipe under plant conditions, Journal of Pressure Vessel Technology, 135 (2013).
[2] R. Viswanathan, J. Henry, J. Tanzosh, G. Stanko, J. Shingledecker, B. Vitalis, R. Purgert, US program on materials technology for ultra-supercritical coal power plants, Journal of materials engineering and performance, 14 (2005) 281-292.
[3] F. Abe, M. Tabuchi, M. Kondo, S. Tsukamoto, Suppression of Type IV fracture and improvement of creep strength of 9Cr steel welded joints by boron addition, International Journal of Pressure Vessels and Piping, 84 (2007) 44-52.
[4] V. Shankar, K. Mariappan, R. Sandhya, M. Mathew, Evaluation of low cycle fatigue damage in grade 91 steel weld joints for high temperature applications, Procedia Engineering, 55 (2013) 128-135.
[5] O. Basquin, The exponential law of endurance tests, in: Proc Am Soc Test Mater, 1910, pp. 625-630.
[6] L. Coffin, Fatigue at high temperature, in: Fatigue at elevated temperatures, ASTM International, 1973.
[7] K. Smith, A stress-strain function for the fatigue of metals, Journal of materials, 5 (1970) 767-778.
[8] K. Tokaji, T. Ogawa, Y. Harada, Z. Ando, Limitations of linear elastic fracture mechanics in respect of small fatigue cracks and microstructure, Fatigue & Fracture of Engineering Materials & Structures, 9 (1986) 1-14.
[9] S. Glodež, B. Aberšek, J. Flašker, Z. Ren, Evaluation of the service life of gears in regard to surface

pitting, Engineering fracture mechanics, 71 (2004) 429-438.
[10] K. Tanaka, T. Mura, A Dislocation Model for Fatigue Crack Initiation, Journal of Applied Mechanics, 48 (1981) 97-103.
[11] K.S. Chan, A microstructure-based fatigue-crack-initiation model, Metallurgical and Materials Transactions A, 34 (2003) 43-58.
[12] X. Wu, On Tanaka-Mura's fatigue crack nucleation model and validation, Fatigue & Fracture of Engineering Materials & Structures, 41 (2018) 894-899.
[13] M. Li, L. Wang, J.D. Almer, Dislocation evolution during tensile deformation in ferritic–martensitic steels revealed by high-energy X-rays, Acta materialia, 76 (2014) 381-393.
[14] R.A. Barrett, P.E. O'Donoghue, S.B. Leen, A physically-based constitutive model for high temperature microstructural degradation under cyclic deformation, International Journal of Fatigue, 100 (2017) 388-406.
[15] R.A. Barrett, P.E. O'Donoghue, S.B. Leen, A physically-based high temperature yield strength model for 9Cr steels, Materials Science and Engineering: A, 730 (2018) 410-424.
[16] J. Earthman, G. Eggeler, B. Ilschner, Deformation and damage processes in a 12% Cr · Mo · V steel under high temperature low cycle fatigue conditions in air and vacuum, Materials Science and Engineering: A, 110 (1989) 103-114.
[17] F. Masuyama, N. Komai, Evaluation of long-term creep rupture strength of tungsten-strengthened advanced 9-12% Cr steels, in: Key Engineering Materials, Trans Tech Publ, 2000, pp. 179-188.
[18] M.N. Batista, M.C. Marinelli, S. Hereñú, I. Alvarez-Armas, The role of microstructure in fatigue crack initiation of 9–12%Cr reduced activation ferritic–martensitic steel, International Journal of Fatigue, 72 (2015) 75-79.
[19] W. Zhang, X. Wang, H. Chen, T. Zhang, J. Gong, Evaluation of the effect of various prior creep-fatigue interaction damages on subsequent tensile and creep properties of 9% Cr steel, International Journal of Fatigue, 125 (2019) 440-453.
[20] X. Wang, T. Zhang, W. Zhang, M.A. Wahab, J. Gong, An improved unified viscoplastic model for modelling low cycle fatigue and creep fatigue interaction loadings of 9–12% Cr steel, European Journal of Mechanics-A/Solids, 85 (2021) 104123.
[21] A.U. Manual, Abaqus Theory Guide. Version 6.14, USA.: Dassault Systemes Simulia Corp, (2014).
[22] T.P. Farragher, S. Scully, N. O'Dowd, S. Leen, Development of life assessment procedures for power plant headers operated under flexible loading scenarios, International Journal of Fatigue, 49 (2013) 50-61.
[23] J. Chaboche, G. Rousselier, On the plastic and viscoplastic constitutive equations—Part I: Rules developed with internal variable concept, (1983).
[24] J.-L. Chaboche, G. Rousselier, On the plastic and viscoplastic constitutive equations—Part II: application of internal variable concepts to the 316 stainless steel, (1983).
[25] M. Li, R.A. Barrett, S. Scully, N.M. Harrison, S.B. Leen, P.E. O'Donoghue, Cyclic plasticity of welded P91 material for simple and complex power plant connections, (2016).
[26] T.P. Farragher, S. Scully, N. O'Dowd, C.J. Hyde, S. Leen, High temperature, low cycle fatigue characterization of P91 weld and heat affected zone material, Journal of Pressure Vessel Technology, 136 (2014).
[27] H. Bhadeshia, Models for the elementary mechanical properties of steel welds, Book-institute of materials, 650 (1997) 229-284.
[28] K. Mariappan, V. Shankar, A.K. Bhaduri, Comparative evaluation of tensile properties of simulated heat affected zones of P91 steel weld joint, Materials at High Temperatures, 37 (2020) 114-128.
[29] C. Pandey, The Characterization of Soft Fine-Grained Heat-Affected Zones in P91 Weldments under Creep Exposure Conditions, steel research international, 91 (2019).
[30] C. Pandey, M.M. Mahapatra, P. Kumar, N. Saini, A. Srivastava, Microstructure and mechanical property relationship for different heat treatment and hydrogen level in multi-pass welded P91 steel joint, Journal of Manufacturing Processes, 28 (2017) 220-234.
[31] T.H. Hyde, W. Sun, Determining high temperature properties of weld materials, JSME International Journal Series A Solid Mechanics and Material Engineering, 43 (2000) 408-414.
[32] M. Touboul, J. Crepin, G. Rousselier, F. Latourte, S. Leclercq, Identification of Local Viscoplastic Properties in P91 Welds from Full Field Measurements at Room Temperature and 625 °C, Experimental

Mechanics, 53 (2012) 455-468.
[33] R. Swindeman, M. Santella, P. Maziasz, B. Roberts, K. Coleman, Issues in replacing Cr–Mo steels and stainless steels with 9Cr–1Mo–V steel, International Journal of Pressure Vessels and Piping, 81 (2004) 507-512.
[34] F. Abe, Analysis of creep rates of tempered martensitic 9% Cr steel based on microstructure evolution, Materials Science and Engineering: A, 510 (2009) 64-69.
[35] U.F. Kocks, A.S. Argon, M.F. Ashby, Thermodynamics and kinetics of slip, (1975).
[36] F. Nabarro, Dislocations in a simple cubic lattice, Proceedings of the Physical Society, 59 (1947) 256.
[37] P.-F. Giroux, Experimental study and simulation of cyclic softening of tempered martensite ferritic steels, in, École Nationale Supérieure des Mines de Paris, 2011.
[38] Y. Wang, R. Kannan, L. Zhang, L. Li, Microstructural analysis of the as-welded heat-affected zone of a grade 91 steel heavy section weldment, Weld. J, 96 (2017) 203-219.
[39] A.S. Khan, S. Huang, Continuum theory of plasticity, John Wiley & Sons, 1995.
[40] A. Saad, C.J. Hyde, W. Sun, T. Hyde, Thermal-mechanical fatigue simulation of a P91 steel in a temperature range of 400–600 C, Materials at High Temperatures, 28 (2011) 212-218.
[41] F.H. Norton, The creep of steel at high temperatures, McGraw-Hill Book Company, Incorporated, 1929.
[42] K. Mariappan, V. Shankar, A.K. Bhaduri, Effect of change in microstructures due to simulation temperatures on the low cycle fatigue behavior of P91 steel, International Journal of Fatigue, 140 (2020).
[43] M. Sauzay, B. Fournier, M. Mottot, A. Pineau, I. Monnet, Cyclic softening of martensitic steels at high temperature—Experiments and physically based modelling, Materials Science and Engineering: A, 483 (2008) 410-414.
[44] V.T. Paul, S. Saroja, P. Hariharan, A. Rajadurai, M. Vijayalakshmi, Identification of microstructural zones and thermal cycles in a weldment of modified 9Cr-1Mo steel, Journal of Materials Science, 42 (2007) 5700-5713.
[45] C.G. Panait, A. Zielińska-Lipiec, T. Koziel, A. Czyrska-Filemonowicz, A.-F. Gourgues-Lorenzon, W. Bendick, Evolution of dislocation density, size of subgrains and MX-type precipitates in a P91 steel during creep and during thermal ageing at 600 C for more than 100,000 h, Materials Science and Engineering: A, 527 (2010) 4062-4069.
[46] P.-F. Giroux, F. Dalle, M. Sauzay, J. Malaplate, B. Fournier, A.-F. Gourgues-Lorenzon, Mechanical and microstructural stability of P92 steel under uniaxial tension at high temperature, Materials Science and Engineering: A, 527 (2010) 3984-3993.
[47] P. Yan, Z. Liu, H. Bao, Y. Weng, W. Liu, Effect of microstructural evolution on high-temperature strength of 9Cr–3W–3Co martensitic heat resistant steel under different aging conditions, Materials Science and Engineering: A, 588 (2013) 22-28.
[48] K. Sawada, M. Takeda, K. Maruyama, R. Ishii, M. Yamada, Y. Nagae, R. Komine, Effect of W on recovery of lath structure during creep of high chromium martensitic steels, Materials Science and Engineering: A, 267 (1999) 19-25.
[49] R. Barrett, T. Farragher, C.J. Hyde, N. O'Dowd, P. O'Donoghue, S.B. Leen, A unified viscoplastic model for high temperature low cycle fatigue of service-aged P91 steel, Journal of Pressure Vessel Technology, 136 (2014).
[50] C.J. Hyde, W. Sun, S.B. Leen, Cyclic thermo-mechanical material modelling and testing of 316 stainless steel, International Journal of Pressure Vessels and Piping, 87 (2010) 365-372.
[51] K. Chandravathi, K. Laha, K. Bhanu Sankara Rao, S. Mannan, Microstructure and tensile properties of modified 9Cr–1Mo steel (grade 91), Materials science and technology, 17 (2001) 559-565.
[52] D.-F. Li, R.A. Barrett, P.E. O'Donoghue, N.P. O'Dowd, S.B. Leen, A multi-scale crystal plasticity model for cyclic plasticity and low-cycle fatigue in a precipitate-strengthened steel at elevated temperature, Journal of the Mechanics and Physics of Solids, 101 (2017) 44-62.
[53] V. Shankar, B. AK, Comparative evaluation of tensile properties of simulated heat affected zones of P91 steel weld joint, Materials at High Temperatures, 37 (2020).
[54] R.A. Barrett, P. O'Donoghue, S.B. Leen, An improved unified viscoplastic constitutive model for strain-rate sensitivity in high temperature fatigue, International Journal of Fatigue, 48 (2013) 192-204.

[55] P. Mac Ardghail, N. Harrison, S. Leen, A process-structure-property model for welding of 9Cr power plant components: The influence of welding process temperatures on in-service cyclic plasticity response, International Journal of Pressure Vessels and Piping, 173 (2019) 26-44.
[56] R.J. Devaney, P.E. O'Donoghue, S.B. Leen, Effect of welding on microstructure and mechanical response of X100Q bainitic steel through nanoindentation, tensile, cyclic plasticity and fatigue characterisation, Materials Science and Engineering: A, 804 (2021) 140728.
[57] D. Long, R. Devaney, P. O'Donoghue, H. Song, R. Barrett, S. Leen, Characterisation of LCF Performance of X100 Weld-Joints: Mechanistic Yield Strength Modelling, Finite Element Analyses and DIC Testing, Journal of Advanced Joining Processes, (2021) 100057.
[58] J. Kramberger, N. Jezernik, P. Göncz, S. Glodež, Extension of the Tanaka–Mura model for fatigue crack initiation in thermally cut martensitic steels, Engineering Fracture Mechanics, 77 (2010) 2040-2050.
[59] P. Mac Ardghail, N. Harrison, S.B. Leen, A through-process, thermomechanical model for predicting welding-induced microstructure evolution and post-weld high-temperature fatigue response, International Journal of Fatigue, 112 (2018) 216-232.